Modelling of FSIs for reactor vessel internals

Authors : Mr. Christoph BLAESIUS (GRS), Joachim Herb (GRS), Juergen Sievers (GRS), Alexander Knospe (TUD), Carsten Lange (TUD)

CORTEX - Contract Number: 754316

Project officer: Foivos MARIAS

Document title	Modelling of FSIs for reactor vessel internals
Author(s)	Mr. Christoph BLAESIUS, Joachim Herb (GRS), Juergen Sievers (GRS), Alexander Knospe (TUD), Carsten Lange (TUD)
Number of pages	57
Document type	Deliverable
Work Package	WP01
Document number	D1.2
Issued by	GRS
Date of completion	2020-02-27 09:49:25
Dissemination level	Public

Summary

Flow-induced mechanical oscillations can be a source of neutron noise. This report contains the description of models to assess the mechanical response of core internals to given excitations. First, a comprehensive overview of known flow-induced mechanical oscillations with effect on neutron flux measurement is given. A mechanical model has been developed, which describes the dynamic behavior of the coupled system of RPV, core barrel and a row of fuel assemblies. Bidirectional effects with the fluid are assessed by a separate hydraulic model. Reduced Order Modelling is employed to transform the model into a state, in which it can be included into neutronic codes.

Approval

Date	By
2020-02-27 09:54:23	Dr. Paolo VINAI (Chalmers)
2020-02-27 09:55:15	Pr. Christophe DEMAZIERE (Chalmers)

Table of Contents

Index of Tables

Table of Figures

Abbreviations

APSD	Auto Power Spectral Density
BOL	Begin of Life
BWR	Boiling Water Reactor
CB	Core Barrel
CFD	Computational Fluid Dynamics
CSA	Cross Sectional Area
DOF	Degree of Freedom
EOL	End of Life
FA	Fuel Assembly
FEM	Finite Element Method
FOM	Full Order Model
FSI	Fluid Structure Interaction
HTP	High Thermal Performance
KWU	Kraftwerk Union
MCP	Main Coolant Pump
MOX	Mixed Oxide Fuel
NPP	Nuclear Power Plant
ODE	Ordinary Differential Equation
POD	Proper Orthogonal Decomposition
PWR	Pressurized Water Reactor
RMS	Root Mean Square
ROM	Reduced Order Model
RPV	Reactor Pressure Vessel
SVD	Singular Value Decomposition
VVER	Water-Water Energetic Reactor

Summary

Flow-induced mechanical oscillations can be a source of noise in neutron flux measurement in NPPs. This report contains the description of models to assess the mechanical response of the RPV and core internals to given excitations. First, a comprehensive overview of known flow-induced mechanical oscillations with effect on neutron flux measurement is given. A mechanical model has been developed, which describes the dynamic behavior of the coupled system of RPV, core barrel and a row of fuel assemblies. Bidirectional effects with the fluid are assessed by a separate hydraulic model. Reduced Order Modelling is employed to transform the model into a state, in which it can be included into neutronic codes.

1   Introduction

Flow-induced mechanical oscillations of the RPV and core internals can affect the neutron flux measured inside and outside the reactor core by moderation and attenuation effects (geometry noise). Neutron flux measurements can e.g. be used to determine mechanical characteristics of components and to detect anomalies and damages at an early stage. Beside individual component vibrations, the mechanically coupled system of RPV and core internals can perform complex core-wide oscillations. Such oscillations are considered as one possible explanation for the observed temporary increase in low-frequency neutron flux noise in KWU type reactors between about 2000 and 2010 for which no fully consistent explanation exists yet (Seidel, et al., 2015), (Herb, et al., 2016).

The work described in this report intends to improve the understanding of the characteristics of flow-induced mechanical oscillation phenomena that influence neutron flux measurements. Therefore, models are developed for the assessment of the dynamic behavior of the core internals under given perturbations, e.g. turbulence, oscillating fluid mass flow profiles or mechanical excitations. The models can be used in conjunction with the neutron kinetic code features developed within the CORTEX subtask 1.2 to compute the neutron flux response to flow-induced mechanical oscillations and compare it to real plant data.

In a first step, literature-known flow-induced mechanical oscillation phenomena, especially those with effect on neutron flux measurements, are summarized and an overview over their characteristics is given. For each phenomenon, associated oscillation modes, the sources of excitation, the visibility in the core instrumentation signals and observed mechanical defects are discussed. The focus is laid on KWU 1300 MWe class PWR, but the results may be transferrable to other PWR and partly VVER.

In a further step, a detailed mechanical model is presented that can simulate the dynamic behavior of the RPV and core internals under given perturbations using the FEM code ANSYS Mechanical. The model benefits from a set of simplifications concerning the structure and the surrounding fluid. Reactive hydraulic forces arising from the component motion itself are e.g. considered by added mass, stiffness and damping values or combined spring and damper elements. Different data sets for the component parameters have been compiled (e.g. for different fuel types and times in the core) to be able to perform parametric studies.

Also, an enhanced version of the thermal hydraulic system code ATHLET has been developed, which allows to simulate effects of fuel assembly movements on the flow in the reactor core, like pressure differences between the interiors of neighboring fuel assemblies generated by their relative movement.

Reduced order modelling is employed on the detailed FEM mechanical model for the reactor core internals to construct low dimensional models appropriate to be coupled with neutron kinetics codes. To this end, applicable methods of model order reduction are investigated. Then all necessary differential equations are extracted from ANSYS Mechanical, transferred to Python and subsequently reduced by the chosen methods of model order reduction.

2 Mechanical oscillations with effect on neutron flux signals

2.1 Detection of mechanical oscillations in neutron flux signals

Current PWR and VVER power reactors are equipped with detectors for the measurement of neutron flux in the operational power range, which are located inside (incore) or outside (excore) the reactor core. Number and type of detectors vary between reactor designs. KWU 1300 MWe class PWRs, e.g., employ eight pairs of counting tubes and ionization chambers outside the core at four quadrants in two altitudes. Inside the core, neutron flux is measured by eight instrumentation tubes at six altitudes, which are discontinuously calibrated by a ball measuring system (Seidel, et al., 2015). While, due to the short diffusion length in the range of a few centimeters, the flux at the incore detectors is dominated by thermal neutrons from the surrounding fuel rods, the excore detectors see fast neutrons, which have been thermalized in the area outside the RPV (Herb, et al., 2016).

The original reason for the neutron flux measurement is the monitoring of the reactor power and power density distribution in the core. For this purpose, the signals are partly normalized and filtered (Reaktorsicherheitskommission, 2013). Investigations showed that the signals and especially its noise components contain additional valuable information about conditions inside the core, where it is impossible or impractical to install diagnostic instrumentation due to limited space, temperature, and radiation (Fry, et al., 1984). Neutron noise analysis was subsequently used for various purposes, such as research on neutron kinetic stability problems (Sunder, 1985), determination of reactivity coefficients, monitoring of thermal hydraulic conditions (pressure pulsations, coolant velocity, subcooled boiling) (Runkel, 1987) as well as monitoring of mechanical properties of core internals and primary circuit components for damage detection (Fry, et al., 1984). The latter, which is based on the effect of periodical change of geometry due to mechanical oscillations (geometry noise), has become an important part of damage monitoring concepts of today's power reactors. For some components, such as fuel assemblies, there even is no further measurement available for the monitoring of mechanical integrity (Sunder, 1985).

Figure 1 gives an overview of core internals performing mechanical oscillations with effect on neutron flux noise measurements in a KWU 1300 MWe class PWR. The mechanical oscillations are visible as distinct peaks in the auto power spectral density (APSD) chart of the neutron flux measurement. Those peaks are overlapped by noise from the inherent stochastic effects of the chain reaction, reactivity noise due to temperature and density variations of the moderator (e.g. subcooled boiling, temperature plumes, transport effects, turbulence) and noise from the detector and signal processing chain. The strength of the peaks depends on the strength of the neutron flux source that is modulated (affected e.g. by fuel type, UO_2 vs. MOX, fuel/moderator-ratio, burnup state), the extent of the mechanical oscillation (affected e.g. by component stiffness, excitation force) and the transfer function between mechanical oscillation and noise measurement (affected e.g. by the neutron diffusion length, the boron/absorber concentration along the path and properties of the detector and signal processing chain).

Source: KTA 3204, 2017
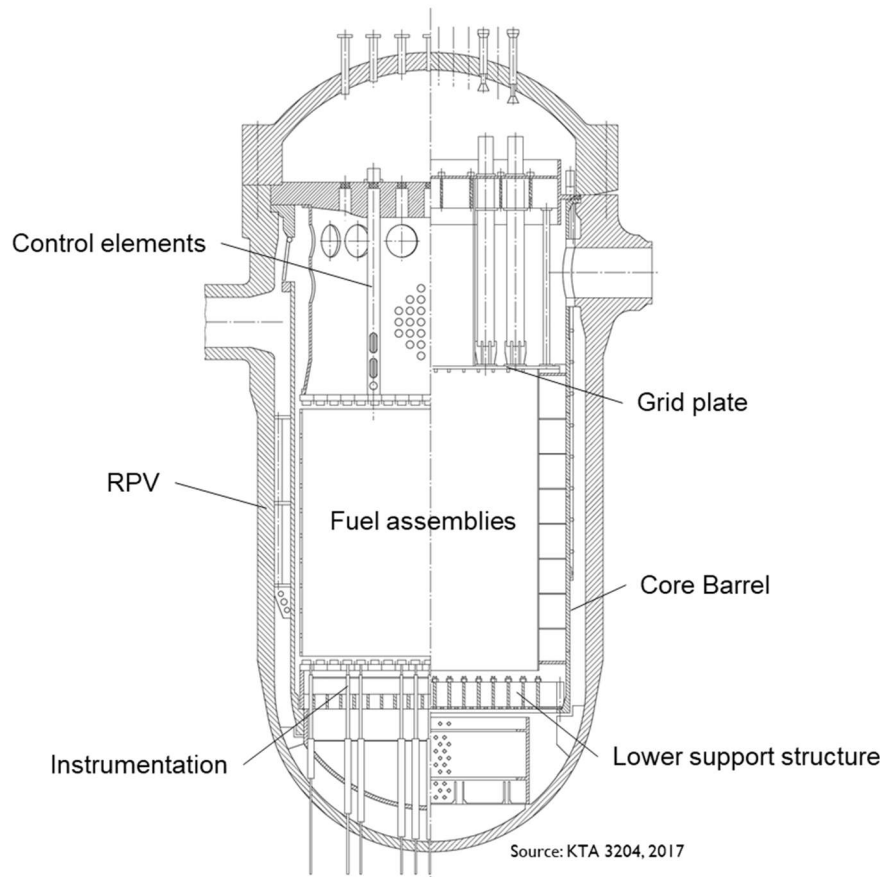
Figure 1: Overview of KWU 1300 MWe class PWR core internals

Apart from the prominent peaks, the correct assignment of signal characteristics to mechanical oscillation modes can be difficult, hypothetical or ambiguous, as they can be weak or visible only in defect-case. Furthermore, apart from isolated individual vibrations, coupled oscillators with partly chaotic characteristics (e.g. double pendulum configurations or collisions) and broadband effects on neutron flux noise exist within the system.

Therefore, the correct assignment is often supported by correlations between different neutron flux sensors or correlations with other sensor types, especially vibration sensors mounted outside the RPV, structure-borne sound measurements or pressure transducers of the primary circuit (Thie, 1981). Mechanical models of the core internals (see section 3.1) and heavily instrumented mock-up experiments, such as the SAFRAN test loop (Damiano & Kryter, 1990) (Au-Yang, et al., 1995) have been used in the past as well. Databases for signal interpretation have been set up, such as the SINBAD database (Trenty, 1995).

Several authors have proposed assignments of neutron flux, vibration measurement and pressure transducer signals to mechanical oscillation modes and other effects, such as (Runkel, 1987) for KWU 1300 MWe class PWR (see Table 1), (Thie, 1981), (Fry, et al., 1984), (Sunder, 1985), (Wach & Sunder, 1988), (Bauernfeind, 1988), (Stegemann & Runkel, 1995) or (Fiedler, 2002). In the following sections, important flow-induced mechanical oscillations with effect on neutron flux measurement are described in detail.

Table 1: Assignment of neutron flux, vibration measurement and pressure transducer signals to mechanical and other oscillations for KWU 1300 MWe class reactor (Runkel, 1987)

Frequency range (Hz)	Analysis Result
0.1 – 0.8	Transport Effect (fluid velocity within FA)
0.8 – 1.0	FA beam mode
1.0 – 1.2	Transport Effect (average fluid velocity in core)
2.6 – 3.5	FA 1st mode both ends clamped
5.3	Standing wave ($\lambda/4$) between RPV and MCP
6.0 – 7.0	FA 2nd mode both ends clamped
7.5	Global fluidic resonance
9.1 – 9.3	RPV/CB out-of-phase mode
10.3 – 10.5	RPV/CB in-phase mode
10.5 – 12.5	FA 3rd mode both ends clamped
12.3 – 12.4	Standing wave (λ_H) between RPV and Pressurizer
12.4	RPV/CB out-of-phase mode
14.7	RPV vertical oscillation
15.0 – 17.0	FA 4th mode both ends clamped
18.1	Standing wave ($\lambda/4$) between Pressurizer and MCP
18.1 – 18.8	CB shell oscillations
24.8	MCP remaining imbalance
26.0 – 30.0	Fuel rod vibrations
29.5	Vibrations of the secondary core support
31.2	Standing wave ($\lambda/2$) between Supporting structure and Pressurizer
39.5	Standing wave ($\lambda/2$) between MCP and CB
44.4	Standing wave ($\lambda/2$) between RPV and Pressurizer
53	Fluidic resonance
75.0	MCP remaining imbalance
81.0	Fluidic resonance
91.0	Fluidic resonance

2.2 Fuel assembly bending oscillations

Regarding oscillation modes, fuel assemblies can be idealized as either cantilevered beam, simply supported beam or simply supported beam with additional fixation at the bottom (Figure 2). Due to their slenderness, fuel assemblies possess the lowest natural frequency among the core internals. For KWU 1300 MWe type PWR, values as low as 0.8 Hz (cantilevered beam mode) and 1.5 Hz (1st mode clamped on both sides) are reported (see section 3.2.2).
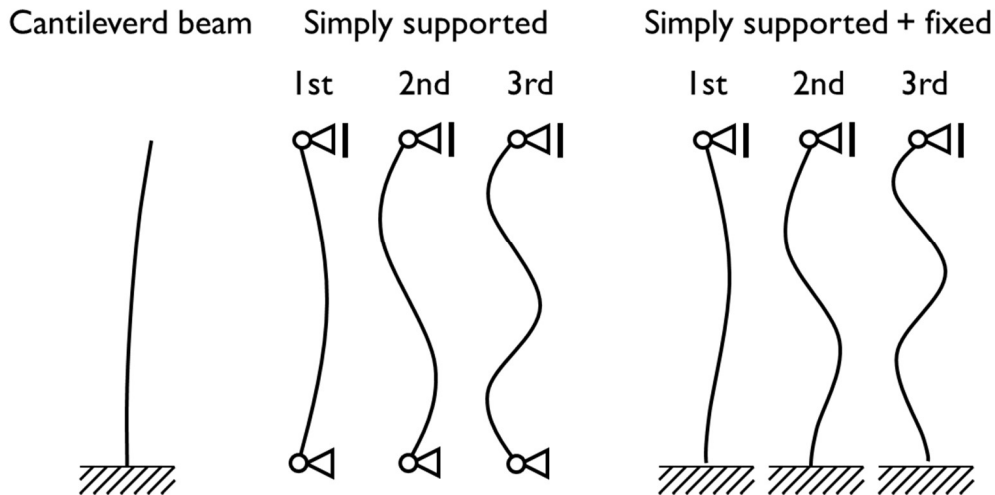
Figure 2: Idealized FA oscillation modes

The real FA oscillation is much more complex, non-linear and cannot be entirely described mathematically due to the complex bearing characteristics and the inhomogeneous stiffness distribution. This e.g. causes a dependency of lateral stiffness and natural frequency from the oscillation amplitude (Sunder, 1985). The weight of the fuel assembly rests on centering pins of the lower support plate, so that the connection is fixed relatively firmly. Nevertheless, a certain rotational freedom at the lower end is provided by elasticity in the bolting of the guide thimbles, a less stiff part of the guide thimble working as shock absorber for the control rods in some designs, and a small lower zone, where the additional stiffening of the fuel rods via the spacers is not effective. In the upper bearing, the location tolerance of the centering pins of about 0.4 mm limits the maximum amplitude of the cantilevered beam mode. Realistic deflection shapes of fuel assemblies for large amplitudes have been measured and simulated in (Ricciardi, 2016), (Wanninger, et al., 2016 b) and (Jeon, et al., 2009) (Figure 3).
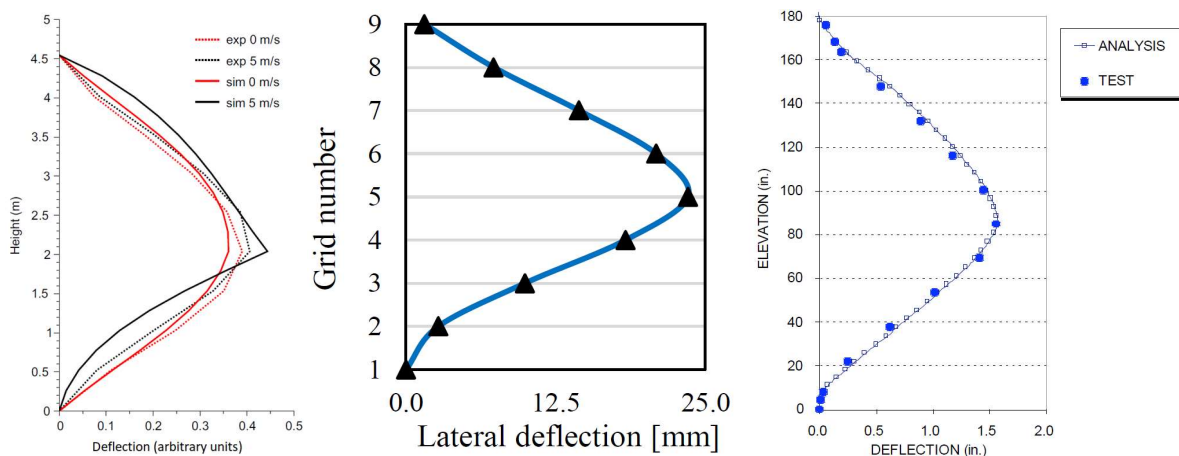
Figure 3: Measured and simulated FA deflection shapes (Ricciardi, 2016), (Wanninger, et al., 2016 b), (Jeon, et al., 2009)

A hard limit for the lateral deflection amplitude of an individual fuel assembly oscillation is the gap between two neighboring fuel assemblies of about 1.6 mm (warm state). In case of accumulated motions of one complete row of fuel assemblies, up to 26 mm deflection is possible (which is achieved only by the outermost fuel assembly) (Pohlus & Paquée, 2018).

During the time in the core, lateral stiffness and mechanical damping of the fuel assemblies significantly decrease. Two main mechanisms are responsible for this behavior. Small springs holding the fuel rods in place within the spacer grids relax with neutron flux (irradiation creep). Consequently, the additional stiffness from the initially tightly connected fuel rods vanishes. This effect is even more distinct for some modern fuel assembly designs, where the springs are not separate parts made from stainless steel, but integral parts of the zirconium-based spacers. In these designs, the spacers at the lowest and highest positions are often made from Inconel steel to reduce this effect (Wanninger, et al., 2016 a). A second mechanism is the different irradiation growth (or even shrinkage) of spacer and fuel rods (irradiation growth/creep), increasing the gap between the spacer and fuel rods, further reducing the contact force of the spring. In extreme cases, contact can be completely lost, and fuel rods slip downwards until their weight is carried only by the contact to the lower part of the fuel assembly (Billerey, 2005), (Wanninger, et al., 2016 a). The contact force and the friction in the spacers are also responsible for the observed hysteresis in displacement, which significantly contributes to the mechanical damping (Collard, 2004). Consequently, the mechanical damping decreases with time in the core as well.

Further mechanisms with minor effect include an increase of Young's Modulus of the guide thimbles due to irradiation, an increase of friction coefficients between spacer springs and fuel rods due to surface oxidation, a change of fuel assembly hold-down force due to creep relaxation of the hold-down springs, and a compression of these springs due to fuel assembly growth (Billerey, 2005). Between laboratory conditions at room temperature and reactor operational conditions, the different coefficient of thermal expansion and the decrease of Young's modulus with temperature are also relevant mechanisms (Wanninger, et al., 2016 a).

In the neutron flux APSD, the width of the peak associated with the first natural frequency indicates the decrease of stiffness over time, since fuel assemblies with different operational time can be found in the core and the natural frequency is strongly correlated with the stiffness. As a rule of thumb, (Trenty, 1995) estimated that the natural frequency of a fresh fuel assembly decreases by 50 % during the first cycle. In (Sunder, 1985) the first three cycles after the initial commissioning of a KWU 1300 MWe class reactor were evaluated and the signal range attributed to the first natural frequency shifted from 5.2 - 3.9 Hz in the first cycle over 4.7 - 3.6 Hz in the second cycle to 4.0 - 3.3 Hz in the third cycle. Thereafter, due to continuous replacement of one third of the core loading after each cycle, no further changes were observed. Further data regarding the development of the lateral stiffness and natural frequencies of the fuel assemblies are described in section 3.2.2.

The fuel assembly vibrations obtain their energy predominantly from fluid mechanic forces (turbulence, lateral flow, pressure pulsations and a changing inlet mass flow pattern) as well as mechanical forces (core barrel motions and collisions amongst each other). In rare cases, which are mainly related to insufficient designs, strong excitation forces, such as jet flow or self-excitation can arise (Runkel, 1987), (Fry, et al., 1984), (Reavis, 1969), (Kim, et al., 2012).

Direct measurements of the average deflection amplitude of the fuel assembly oscillations under operational conditions are rare due to the obvious difficulties with such measurements. (Pohlus & Paquée, 2018) made a rough estimation by taking signals of a single broken fuel assembly, which was roughly ten times increased compared to intact fuel, as a basis and assigned the value to an amplitude in the order of the gap between fuel assemblies (1.6 mm). By implication, the maximum amplitude of an intact fuel assembly was estimated a tenth of this gap (0.16 mm) with an average

variation about three times smaller (0.05 mm). In (Runkel, et al., 1995) and (Laggiard, et al., 1995) actual accelerometer measurements with miniature incore probes were performed in a KWU 350 MWe class PWR. The RMS of the deflection was determined to be 0.035 mm, which means that a displacement of 0.035 mm is exceeded averagely 6869 times per hour and a displacement of 0.137 mm 2.2 times per hour. (Fry, et al., 1984) reconstructed fuel assembly oscillation amplitudes from ex-core detector neutron noise at Sequoyah 1 PWR. The reconstructed amplitudes could be separated into a correlated part amongst all fuel assemblies (0.37 µm RMS) and an uncorrelated part (3.1 µm RMS).

Fuel assembly oscillations can modulate neutron flux in different ways that encompass the change of moderator/absorber/fuel ratio and distribution, the change of the distance between source and detector, the relative movement in temperature plumes or bypass flows, the motion of the detector in a neutron flux gradient, the change of the reflector thickness at the core edge or indirect effects via thermal hydraulic parameters (Runkel, 1987), (Herb, et al., 2016).

The signals of the predominantly uncorrelated motion of the fuel assemblies largely compensate each other in the excore detector signals and a clear identification is usually possible only by incore detectors. The main identification criterion is an in-phase behavior of sensors at different altitudes (Runkel, 1987), (Fiedler, 2002). (Sunder, 1985) concluded that at least the outermost fuel assemblies can be (weakly) seen in excore detectors (Figure 4). While (Sunder, 1985) did not find the signal in vibration sensors mounted to the RPV and pressure transducers, (Runkel, 1987) concluded that at least the coherent part of the lowest modes can be detected there.
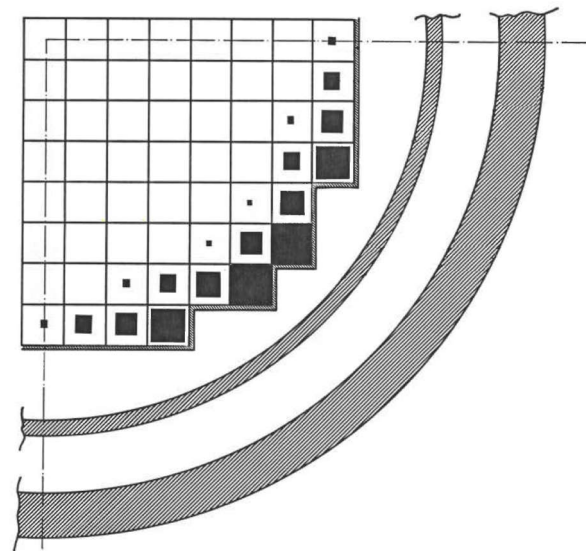
Figure 4: Visibility of FAs in excore detectors, area proportional to signal (Sunder, 1985)

Defects of the fuel assemblies reported in literature encompass e.g. the break of a hold-down spring or the loosening of a guide thimble fixation (Runkel, 1987). Mechanical defects can influence the form, amplitude and frequency of the oscillation. Strong unexpected oscillations involving self-excitation mechanisms were reported for fuel assemblies of an experimental fast breeder reactor in (Mitzel, et al., 1982) and a novel fuel assembly design during a flow-sweep-test in (Haslinger, et al., 2001).

2.3 RPV and core barrel oscillations

The RPV and core barrel oscillations can be idealized as pendulum-like oscillators, since the body of the components is rather stiff, and the flexibility is concentrated in the upper bearing. While the RPV is mounted to an external rigid structure via support lugs, the core barrel is mounted to the RPV via hold-down clamps and a supporting plate. Gravity plays only a minor role in the pendulum motion since the energy predominately oscillates between kinetic energy and deformation energy of the bearing. A certain damping comes from the bearing and the fluid in the downcomer (Wach & Sunder, 1977). Figure 5 shows a model of the coupled system according to (Bauernfeind, 1977).
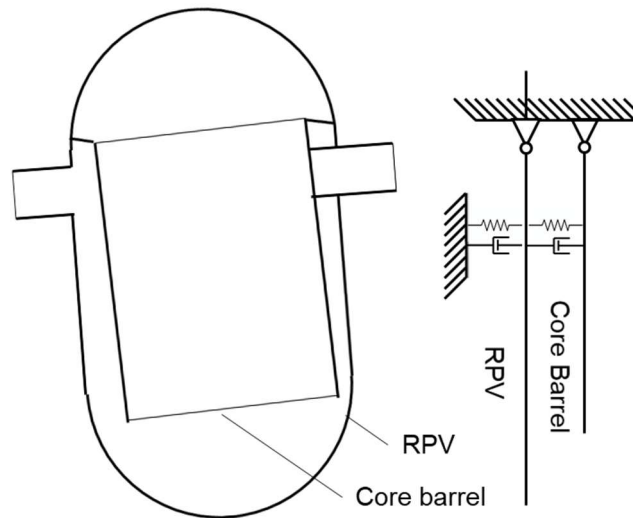
Figure 5: Coupled system of RPV and core barrel pendula according to (Bauernfeind, 1977)

The coupled system can oscillate in two basic modes, in-phase and out-of-phase (Figure 6). For the out-of-phase mode a natural frequency of 7.4-9.3 Hz is reported depending on the oscillation direction for a KWU 1300 MWe class PWR. In-phase modes are found in the range of 10.3-12.4 Hz (Runkel, 1987), (Fiedler, 2002). (Sunder, 1985) reconstructed trajectories of the components and observed that motions of the core barrel could be detected in the RPV motion with a time delay. The out-of-phase mode is strongly influenced by the fluid in the annular gap. (Altstadt & Weiss, 1999) modelled this effect and calculated natural frequencies of 13.7 Hz vs. 26.3 Hz with/without consideration of the fluid-structure interaction in the annular gap.

Out-of-phase mode   In-phase mode
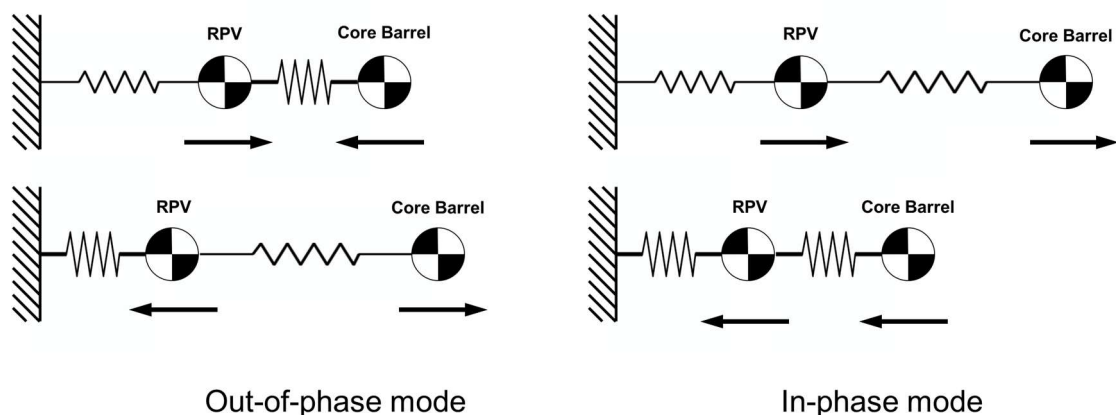
Figure 6: Schematic representation of the modes of the coupled system of RPV and core barrel

The RPV further performs vertical oscillations at a frequency of around 14.7 Hz (KWU 1300 MWe class PWR). The core barrel further performs shell oscillations, which can be separated into shell mode and global mode (Figure 7). The latter one is more distinct in neutron flux measurements and reported at 18.1-22 Hz for a KWU 1300 MWe class PWR (Runkel, 1987).
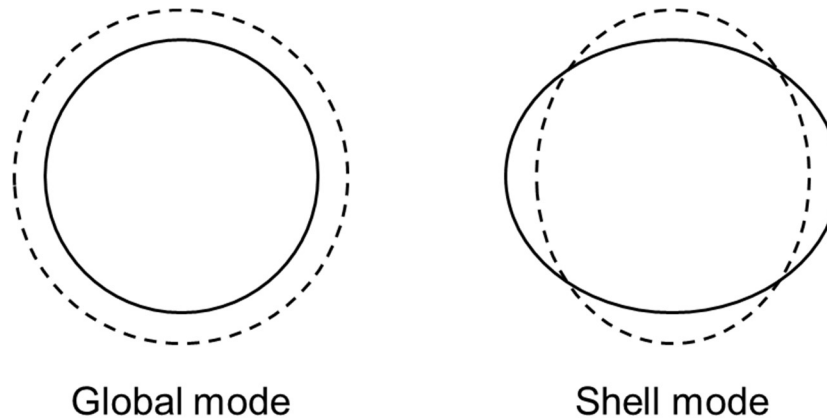
Figure 7: Schematic representation of the global and shell mode of the core barrel

The RPV and core barrel oscillations are excited mainly by stochastic fluid forces in the annular gap, such as turbulence, pressure fluctuations as well as fluid dynamic forces from fluid deflection at the gap inlet and outlet (Runkel, 1987), (Snyder, et al., 2004), (Wei, 2015).

Apart from stochastically excited oscillations at natural frequency, the coupled system of RPV and core barrel, particularly the out-of-phase pendulum and the shell mode, are strongly prone to forced oscillations due to pressure pulsations. This makes it possible to detect further effects in neutron flux measurements, which are transferred via fluid pressure (see sections 2.4.4, 2.4.5, 2.4.6, 2.4.7 and 2.4.8). The response to pressure pulsations can be further amplified when the excitation frequency is close to a natural frequency of the oscillation modes (Runkel, 1987).

Like for the fuel assemblies, direct measurements of the average deflection under operational conditions are rare. (Thie, 1981) reconstructed the RMS of the motion from neutron flux noise signals as typically 0.02 mm to 0.06 mm. Incore accelerometer measurements in (Laggiard, et al., 1995) on a KWU 350 MWe class PWR yielded an RMS of 0.027 mm.

The strongest transfer mechanism of the RPV/core barrel oscillations to the neutron flux measurements is the modulation of the reflector thickness in form of the annular gap and its moderation and absorption capabilities. The change of the distance between source and detector may have an additional, but probably smaller effect (Runkel, 1987). Via the lower support plate and the upper grid plate, the movements are also transmitted as 'base point excitations' to the fuel assemblies, which themselves have effects on neutron flux measurements (see section 2.2) (Sunder, 1985). While the out-of-phase pendulum mode and the shell mode are especially prone to excitation by pressure pulsations, the effect is also existent in the opposite direction, which means that the mechanical oscillations could be observed in the pressure transducers signal (Runkel, 1987).

Oscillations of the coupled RPV/core pendulum system can be identified as two or more peaks in the APSD of the excore detectors (Fiedler 2002). A specific characteristic is the 180°-phase-shift of

opposite detectors. The signal of the in-phase mode is weaker compared to the out-of-phase mode. The pendulum motion can be identified in the incore sensors as correlated fuel assembly excitations (Sunder, 1985). The pendulum oscillations can be further detected in vibration sensors mounted outside the RPV and pressure transducers (Runkel, 1987).

During normal operation, when all control rods are pulled out of the core, the RPV vertical mode is only visible in the RPV-mounted vibration sensors (strong correlation and no phase-shift between the sensors). The core barrel shell and global mode are visible in excore neutron flux detectors and can be separated by correlation analysis between the sensors at the four quadrants. A strong visibility is further reported for pressure transducers. The signal could not be identified in incore neutron flux measurements and vibration sensors (Sunder, 1985).

The identification of a core barrel defect in the Palisades NPP was one of the first applications of neutron flux noise analysis in the field of damage detection (Fry, et al., 1974). Further cases are reported in (Liewers, et al., 1988), (Damiano & Kryter, 1990), (Altstadt & Weiss, 1999) and (Schumann, 2000). Cases of relaxed hold-down springs or insufficient bolt pre-load resulted in a frequency shift. Cases with a complete loss of fixation resulted in a "rocking" motion of the core barrel rather than a harmonic oscillation. In this case, collisions with the RPV introduced chaotic aspects into the motion behavior (Liewers, et al., 1988).

2.4 Further oscillations with weak, indirect or only defect-related effect

2.4.1 Fuel rod bending oscillations

The individual fuel rods can be excited to bending oscillations. The mode of oscillation is determined by the distance between the spacers and the bearing therein (Figure 8). In KWU 1300 MWe class PWR frequencies of 26 - 30 Hz have been reported (Fiedler, 2002). The oscillation is usually excited by turbulence and energy transfer from the fuel assembly oscillations (Kim, et al., 2012). The amplitudes are rather small, in the range of 10^{-3} to 10^{-2} of the diameter of the rod (Païdoussis, 2016). The fuel rod oscillation can be regarded isolated from a mechanical point of view, since they are not part of the oscillation system RPV/core barrel/fuel assemblies. A signal is usually only visible in the case of a defect close to an in-core detector (Runkel, 1987).

Figure 8: Schematic representation of the fuel rod oscillation mode

Fuel rod oscillations are the main cause of Grid to Rod Fretting (GTRF), an abrasion process between spacer and fuel rods. In extreme cases radioactive material can be released (Païdoussis, 2016). Significant effort has been put into the modelling and prevention of this process (Elmahdi, et al., 2011).

A failure of a single spacer bearing is described in (Sunder, 1985). The failure led to a doubling of the vibrating section length and thus a halving of the corresponding oscillation frequency. The failure was located easily, since it was close to an incore neutron flux detector. A specific kind of flow-induced vibration of fuel rods at the outer core boundary, termed "Baffle Jetting", historically occurred

in reactor designs with a countercurrent flow configuration in the bypass region. Increased gaps between baffle plates and the differential pressure lead to jet flows directed radially towards the core. These flows caused vibrations and damage at the outermost fuel rods of the fuel assemblies near the baffle gaps (O'Cain, 2013). The effect is discussed in detail in (Fujita, 1990) and (Damiano & Kryter, 1990).

2.4.2   Control elements/rods oscillations

Mechanical oscillations of the control elements concern either the components itself or the drive mechanisms. For KWU 1300 MWe class PWR natural frequencies were reported at 3.5 Hz (1st mode) and 17.5 Hz (2nd mode) (Wehling, et al., 1985). During normal operation, when control rods are pulled completely out of the core, no effect on neutron flux can be observed. In special operating conditions with partially inserted control rods, the oscillations modulate the water gap around the absorber and can be clearly observed in incore and excore neutron flux detectors with a coherence of the sensors at different altitudes (Runkel, 1987).

Defects of the control rods encompass bearing damages, broken control rod spiders or other broken parts of the component (Damiano & Kryter, 1990), (Demazière, 2017). Especially in VVER reactors, cases of excessive flow-induced vibrations were observed leading to mechanical damage (Schumann, 2000). Due to the construction of the control elements as double pendulum configuration and collisions with the walls, the signal showed a chaotic characteristic (Hollstein, 1995).

2.4.3   Instrumentation oscillations

Mechanical oscillations of neutron flux instrumentation tubes itself or other instrumentation can be visible in incore sensors (Runkel, 1987). Cases of specific defects were reported in (Damiano & Kryter, 1990) and (Païdoussis, 2006). Similar defects were also observed in BWR type reactors (Damiano & Kryter, 1990), (Païdoussis, 2006) and (Demazière, 2017).

2.4.4   Oscillations of other incore structures

The mechanical oscillations of several incore structures can have an indirect effect on neutron flux measurement due to a mechanical coupling with fuel assemblies, core barrel or RPV. In some older PWR, a thermal shield in form of a core-height steel cylinder outside the core barrel (Figure 9) is part of the oscillation system RPV/core barrel. It is standing upright on the RPV bottom performing 'wobbling' oscillations where the lower end remains round due to the connection with the RPV and the upper end performs shell-like oscillation (Sunder, 1985). A frequency of 3,2 - 4,5 Hz is associated with this oscillation in a KWU 1300 MWe class PWR (Runkel, 1987). Oscillations are visible in incore and excore detectors as well as in vibration sensors and pressure transducers (Runkel, 1987).
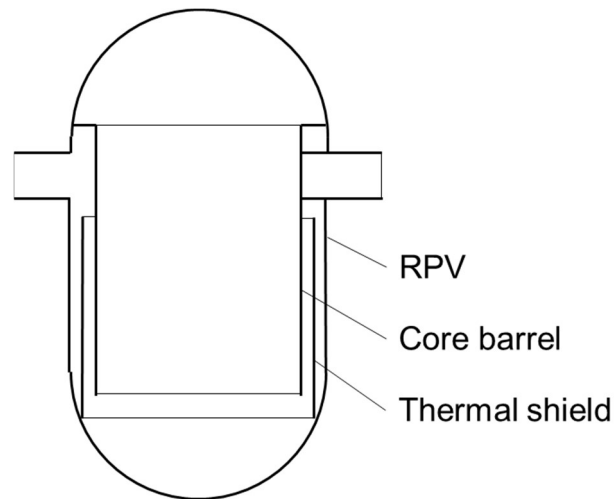
Figure 9: Schematic representation of reactor internals including the thermal shield

Common reported defects concerning the thermal shield are the loosening of the component fixation (Damiano & Kryter, 1990) or large-amplitude self-excited oscillations based on the phenomenon of leakage flow in the annular passage (Mulcahy, 1983). The latter effect, involving a periodic interaction between fluid flow and flow passage cross section is described in more detail in (Païdoussis, 2006) and (Kaneko, 2014).

The purpose of the secondary core support (Figure 13) is the fall protection for the core barrel and its internals. Under normal operation conditions, the secondary core support has no contact to the core barrel and is fixed only to the RPV. The component performs direction dependent bending and torsional oscillations at 29.3-29.8 Hz, respectively 39 Hz in KWU 1300 MWe class PWR (Fiedler, 2002) (Wehling, et al., 1985). It forms a coupled oscillation system with the RPV, making the oscillations visible in the vibration sensors mounted outside the RPV (Runkel, 1987). In newer KWU reactors it is replaced by a flow skirt (Fiedler, 2002). Defects concerned e.g. loose bolting (Damiano & Kryter, 1990), (Stegemann & Runkel, 1995).

The upper grid plate and lower support structure (Figure 1) hold the fuel assemblies in place. They perform a membrane oscillation with effect on the fuel assemblies and core barrel, making it visible in pressure transducers and vibration sensors during normal operation (Runkel, 1987).

2.4.5 *Oscillations of supporting structures and primary circuit components*

Similar to core internals, oscillations of supporting structures and primary circuit components outside the RPV can have an indirect effect on measurements as well. Motions are transferred via mechanical couplings or pressure pulsations. (Stegemann & Runkel, 1995) found even ground motions caused by neighboring aggregates in neutron flux signals. (Wehling, et al., 1985) listed numerous oscillation modes of primary circuit piping, main coolant pump and steam generator. The most prominent oscillation is the pendulum oscillation of the steam generators around 1 Hz (Wach & Sunder, 1988), (Bauernfeind, 1988). This makes it possible to identify failures in the steam generator bearing (Altstadt, et al., 1997). (Damiano & Kryter, 1990) further described the possibility to identify cracked piping due to a change in oscillation frequency.

2.4.6 Pressure pulsations generated by the main coolant pump

As described in section 2.3, some oscillation modes of the RPV/core barrel system are especially prone to be excited by pressure pulsations. One of the strongest forced excitations comes from remaining imbalances of the main coolant pump. The effect can be identified as a sharp peak between 24.8 and 25 Hz in the APSD of both incore and excore neutron flux signal as well as in vibration sensors and pressure transducers (Runkel, 1987). (Fiedler, 2002) identified a further subharmonic mode at 12.5 Hz. The frequency is an almost integer divisor of the grid frequency, since the main coolant pump is driven by an induction motor. The strong signal makes it possible to detect irregularities in the pump function, such as large imbalances, cracks in the pump shaft and bearing damages (Stegemann & Runkel, 1995). A second effect stemming from the main coolant pump concerns acoustic pressure pulsations from passing pump blades at high frequencies (Banyay, et al., 2013).

2.4.7 Standing waves in the primary circuit piping

A hydraulic oscillation phenomenon, which can be also indirectly observed in all neutron flux measurement signals and especially in pressure transducers, concerns standing waves (Sunder, 1985), (Fiedler, 2002) (Figure 10). The frequency of the waves depends on the length of the channel and the configuration of its ends. As the average coolant temperature decreases, the frequencies shift upwards according to the increase in the speed of sound and thus can be distinguished from pressure pulsations induced by component vibrations (Runkel, 1987). (Runkel, 1987), (Fiedler, 2002) and (Seidel, et al., 2015) listed corresponding peaks in the pressure transducer APSD signal, starting from 5.3 Hz.
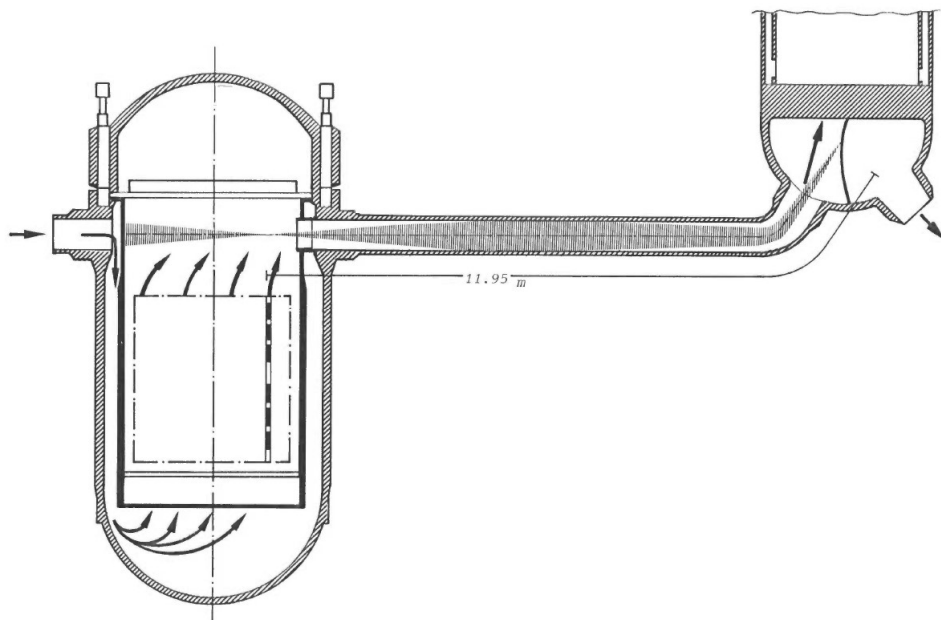
Figure 10: Standing wave between RPV and steam generator (Sunder, 1985)

2.4.8 Cavity resonances of unexpected gas volumes

Unexpected gas volumes in the RPV can initiate a cavity resonance oscillation, which modulates neutron flux in the core via a global reactivity effect (Runkel, 1987). A cavity resonance is characterized by an oscillation of energy between pressure in the cavities and kinetic energy of the fluid (Figure 11). (Fiedler, 2002) attributed a signal in the pressure transducers of a KWU 1300 MWe class PWR at around 0.5-1 Hz to a hypothetical cavity resonance between the pressurizer gas volume and an unidentified gas volume in the RPV, possibly subcooled boiling. The signal showed an in-phase behavior between all sensors. The amplitude was higher for the loop encompassing the pressurizer. A signal around 7.5 Hz is sometimes attributed to a cavity resonance as well (Runkel, 1987), (Seidel, et al., 2015).
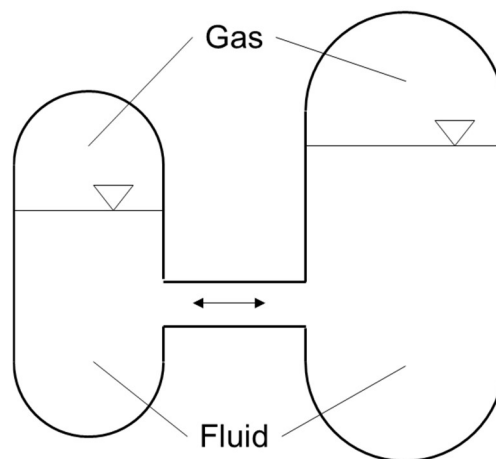
Figure 11: Schematic representation of a cavity resonance

3 Detailed modelling of the core internals dynamic behavior

3.1 Modelling of core internal dynamic behavior in literature

Models of the dynamic behavior of fuel assemblies have been developed for various purposes and in various detail. Simple models are typically used for seismic analysis (Figure 12). More sophisticated models, as described e.g. in (Wanninger, et al., 2016 a) are able to consider internal mechanical processes such as contacts and friction. Some of the models include reactive effects of the surrounding fluid, which is achieved either in form of added mass, stiffness and damping values or more complex expressions (Ricciardi, 2016). Models considering a full reactor core and the fluidic coupling between fuel assemblies are e.g. proposed by (Broc, et al., 2003). In some models, the interaction between fluid flow and structure is modelled using homogenization methods and porous media (Ricciardi, et al., 2009). A more comprehensive review of fuel assembly modelling in literature is given in (Fontaine & Politopoulos, 2000) and (Ricciardi, et al., 2009).
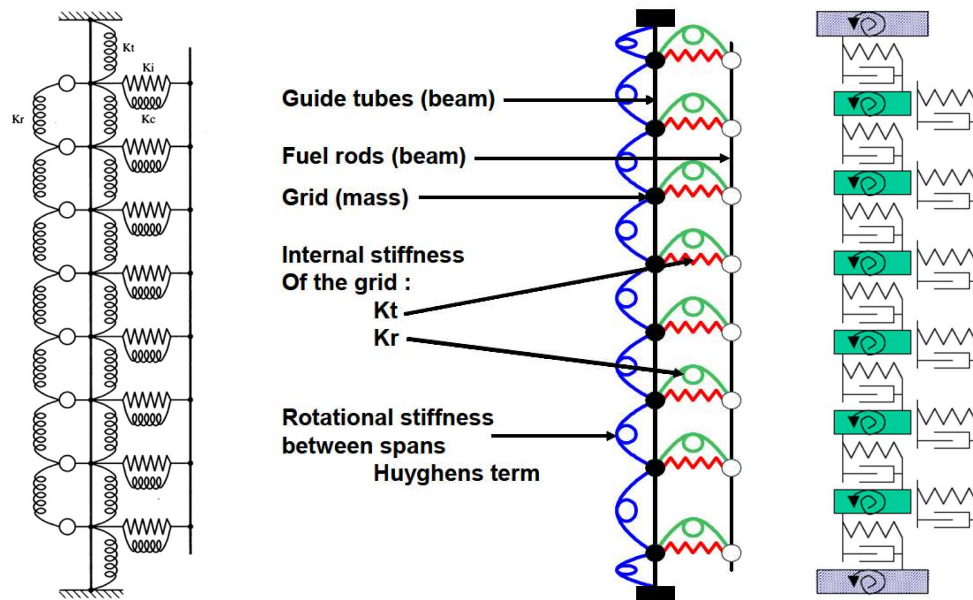
Figure 12: Fuel assembly dynamic models for seismic analysis in (Fontaine & Politopoulos, 2000), (Viallet, et al., 2003) and (Collard, 2004)

RPV and core barrel dynamic behavior has been modelled in literature e.g. to evaluate the motions induced by turbulence in the annular gap for new reactors in (Snyder, et al., 2003) and (Palamera, et al., 2015).

Models of mechanically coupled core internals for the specific purpose of identifying and interpreting measured oscillations, e.g. in neutron flux, were first developed by (Bauernfeind, 1977) (Figure 13). In his work, mechanical parameters were tuned to eigenfrequencies found during pump shutdown tests. (Wach & Sunder, 1977) and (Bauernfeind, 1988) modified the models and included additional mechanical oscillators (Figure 14). Mechanical parameters were additionally obtained from manufacturer's data and shaker table tests. The models were used to identify and interpret measured oscillations as well as to simulate the effect of mechanical failures on the measured signals, such as relaxed core barrel hold-down springs (Damiano & Kryter, 1990). Similar models were developed for VVER in (Dach, et al., 1985) and (Altstadt & Weiss, 1999).
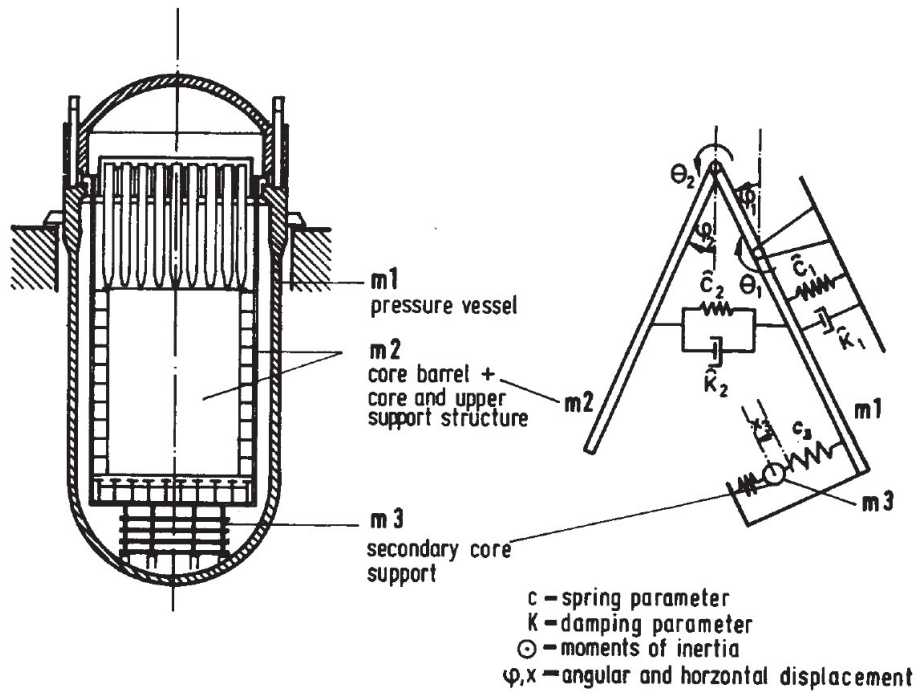
Figure 13: Model of the coupled system of RPV and core barrel pendula (Bauernfeind, 1977)
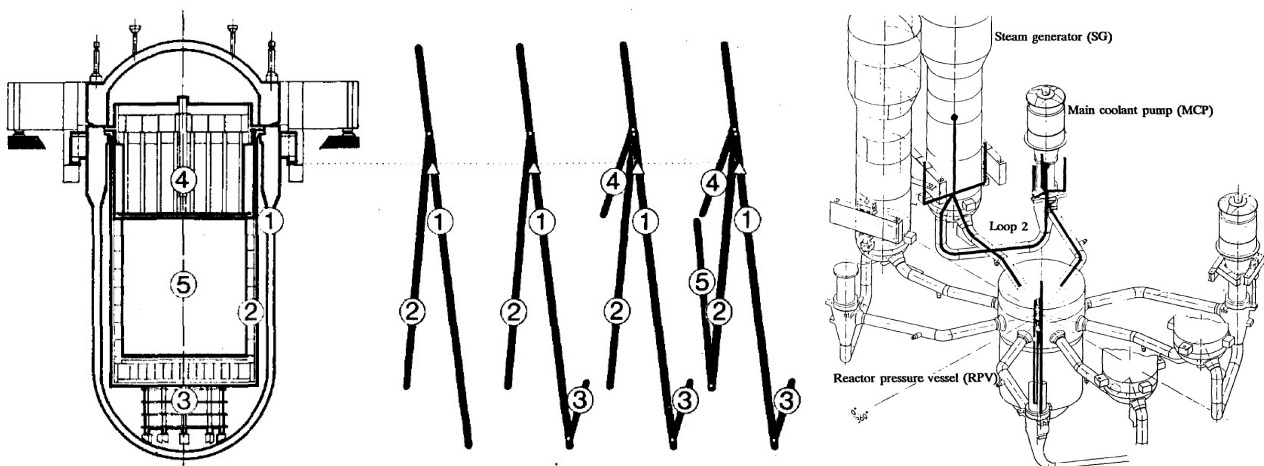
Figure 14: Model of the coupled system of core internals (Wach & Sunder, 1977) and primary circuit components (Bauernfeind, 1988)

3.2 Mechanical model based on ANSYS Mechanical

3.2.1 General approach

The model presented in this section, which was developed by GRS, is based on the idea of (Bauernfeind, 1977) and describes the dynamic behavior of the RPV and core internals in the time domain (central box in Figure 15). It combines a simple modeling approach with a better resolution of the entirety of fuel assemblies, a consideration of reactive fluidic effects and an embedding into a multidisciplinary environment.
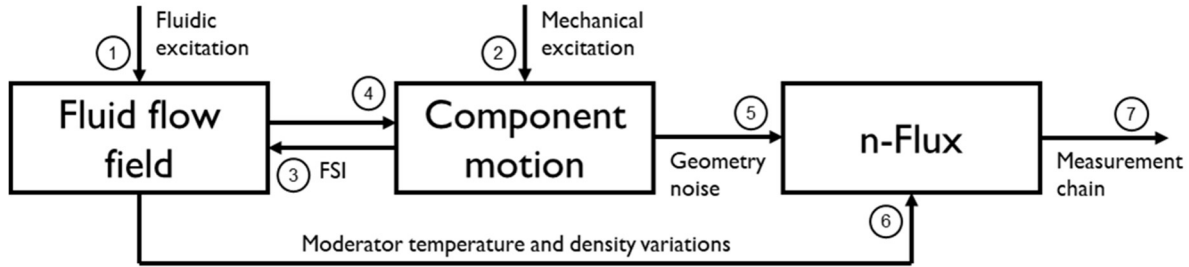
Figure 15: Schematic representation of the relations between the disciplines

The genesis of primary excitation forces, either of fluidic or mechanical nature (arrows 1 and 2 in Figure 15), is not modelled, since they encompass a wide field of known and hypothetical phenomena including turbulence, oscillating fluid mass-flow profiles and mechanical excitations. Instead, generic excitation forces, each of which represents a class of phenomena, can be directly applied to the mechanical model. These generic forces may include:

- Test forces: An initial deviation of one oscillator by a realistic quantity can be used to get an impression of the systems basic transient and steady-state behavior (section 3.2.4).
- Known stochastic forces: Measured and calculated turbulence spectra for fuel assemblies and core barrel are e.g. described in (Snyder, et al., 2004) and (Wei, 2015).
- Known periodic forces: Frequency and amplitude of the excitation forces of RPV and core barrel due to coolant pump pressure oscillations or large eddies in the annular gap are given e.g. in (Zeman & Hlavác, 2008) and (Altstadt, et al., 1997).
- Hypothetical excitation forces: The application of a broad variety of excitation forces may reveal unknown flow-induced vibration effects as well as hidden characteristics of the system, such as chaotic aspects, that may be associated with observations in neutron flux measurements.
- In the special case of self-induced oscillations, the oscillation of the system may arise from the bidirectional interplay between fluid flow field and component itself without the need for a primary excitation.

The interaction between fluid and structure is bidirectional in nature (arrows 3 and 4 in Figure 15). Reactive (secondary) fluidic forces, which are caused by the oscillator deviation itself, can be included into the model in a linearized manner in terms of added mass, added damping and added stiffness (Borsoi, 2001), i.e.:

$$m_s * \ddot{x}(t) + c_s * \dot{x}(t) + k_s * x(t) = f_t(t) + f_{fs}(\ddot{x}, \dot{x}, x) \tag{1}$$

$$[m_s + m_{fs}] * \ddot{x}(t) + [c_s + c_{fs}] * \dot{x}(t) + [k_s + k_{fs}] * x(t) = f_t(t) \tag{2}$$

where m_s is the real and m_{fs} the added mass, c_s is the real and c_{fs} the added damping, k_s is the real and k_{fs} the added stiffness, x the oscillator position, t the time, f_t the sum of the excitation forces and f_{fs} the fluidic forces.

Fluidic effects also encompass the coupling between components, e.g. between RPV and core barrel in the annular gap and the coupling between neighboring fuel assemblies. In the model, these fluidic couplings are considered using combined spring and damper elements.

To obtain a first set of values for fluid-induced added mass, stiffness and damping, literature data from shaker table tests and corresponding calculations are used, which have been performed in conjunction with seismic analysis on single fuel assemblies in axial flow.

Nevertheless, these values are not fixed properties of the system, but significantly depend on the type of excitation and boundary conditions (Stabel, et al., 2005). The fluid-induced added damping, e.g., might vanish for an excitation by a periodically changing mass flow profile, when the relative motion between fluid and structure vanishes as well. Added mass and stiffness have been shown significantly dependent on the confinement of the flow. For self-induced oscillations even negative added values could arise.

The separate hydraulic model (section 3.2.4) can be used to determine the fluidic response (arrow 3 in Figure 15) and the moderator temperature and density variations (arrow 6 in Figure 15) in a more detailed manner or for further excitation types and boundary conditions. A bidirectional coupling to the mechanical model is not implemented at this stage.

The trajectories calculated with the mechanical model (arrow 5 in Figure 15) can be used in conjunction with the neutron kinetic code features developed within the CORTEX subtask 1.2 to calculate the neutron flux response (arrow 7 in Figure 15) and compare it to real plant data.

3.2.2 Model of a single fuel assembly

Figure 16 shows the mechanical model of a single fuel assembly. The fuel assembly structure is represented by a flexible beam. Internal structures are not resolved. Longitudinal growth due to irradiation is neglected. The bearing of the beam is chosen simply supported on both ends with an additional torsion spring at the bottom and an allowed vertical translation at the upper bearing. Using the symmetry of the model, all motions normal to the paper plane are suppressed. The beam is discretized into 20 finite elements.
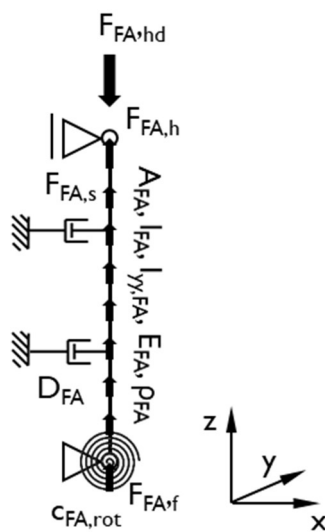
Figure 16: GRS-model of a single fuel assembly

The weight is evenly distributed over the beam length by choosing appropriate values for cross section A, while assuming a realistic material density ρ. All area moments of inertia except the one responsible for bending in the paper plane I_{yy} are chosen sufficiently stiff.

While assuming a realistic Young's modulus E, the area of momentum in the plane I_{yy} is iteratively adapted to achieve the specific lateral stiffness of the fuel assembly (Table 2). The lateral stiffness of the fuel assembly is the central parameter determining the oscillation characteristics of the fuel assembly. Tuning of mechanical parameters to measured data is a common practice for dynamic models of core internals (Altstadt, et al., 1997), (Zeman & Hlavác, 2008), (Jeon, et al., 2009). Optionally, the stiffness can be partially attributed to the torsional spring c_{rot} to obtain a more realistic form of deformation (Figure 3).

Volume forces from gravity and buoyancy are neglected due to their comparably small size. An appropriate hold-down force is applied to the top of the beam. The relaxation of the hold-down spring forces during the time in the core is not considered in a first approach. Axial hydraulic forces arising through the hydraulic flow resistance of spacers and other structural parts are considered using design values. Lateral hydraulic forces are neglected, since the influence on oscillatory behavior is estimated low when lateral contacts between fuel assemblies are not considered.

A set of damper elements at different heights is attached between the fuel assembly and the environment, assuming that the majority of the fuel assembly damping is due to fluid and depends on the absolute velocity. The vertical distances between the damper elements are chosen appropriately to avoid integer ratios that could lead to an impressing of higher oscillation modes.

For the determination of the lateral stiffness of the fuel assemblies, a literature review has been carried out (Figure 17). The reported values describe a deflection resulting from a single force in the middle of the fuel assembly. The collected data can be coarsely divided into three groups. Group A can be associated with conventional fuel assembly designs. A special characteristic is the bilinear course of the stiffness with different values for deflections below and above about 4 mm. Group B can be associated with modern fuel assembly designs (e.g. Areva HTP) in a fresh state respectively at BOC. For this group, the deflection curve shows a pronounced hysteresis. Group C describes data for modern fuel assemblies at EOC as well as measurements on pure fuel assembly skeletons. As mentioned in section 2.2, contact forces between spacer and fuel rods decrease during the time in the core. The additional stiffness from contact and the damping from the hysteresis vanishes and the lateral stiffnesses of fuel assembly and skeleton converge.

Data from shaker table tests and corresponding calculations, which were performed in conjunction with seismic analysis, showed only moderate values for added mass and added stiffness (Figure 18, Figure 19). This is further supported by the measured small difference of natural frequencies measured between air and (flowing) water (Figure 20). As discussed in 3.2.1, the validity of this assumption may be given only for similar excitation types and boundary conditions as in the shaker table tests.
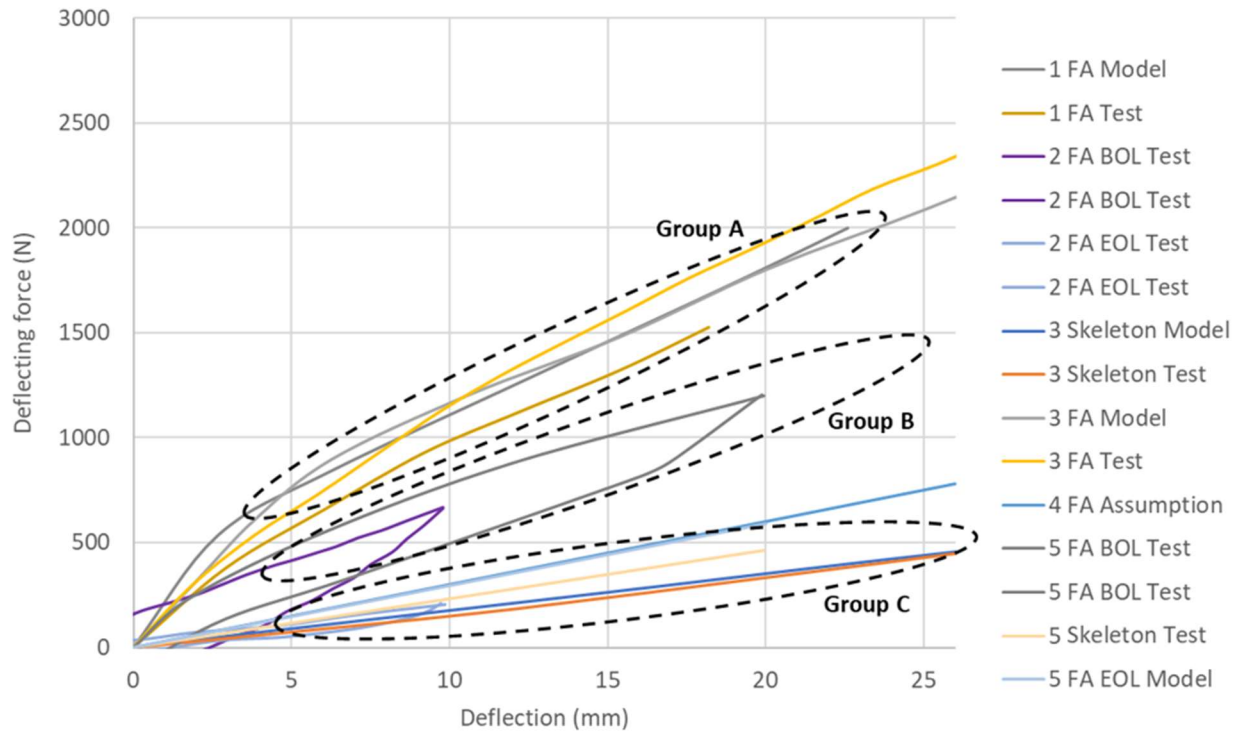
Figure 17: Values for FA lateral stiffness in 1: (Fontaine & Politopoulos, 2000), 2: (Collard, 2004), 3: (Jeon, et al., 2009), 4: (Horváth & Dressel, 2013) and 5: (Wanninger, et al., 2016 b)
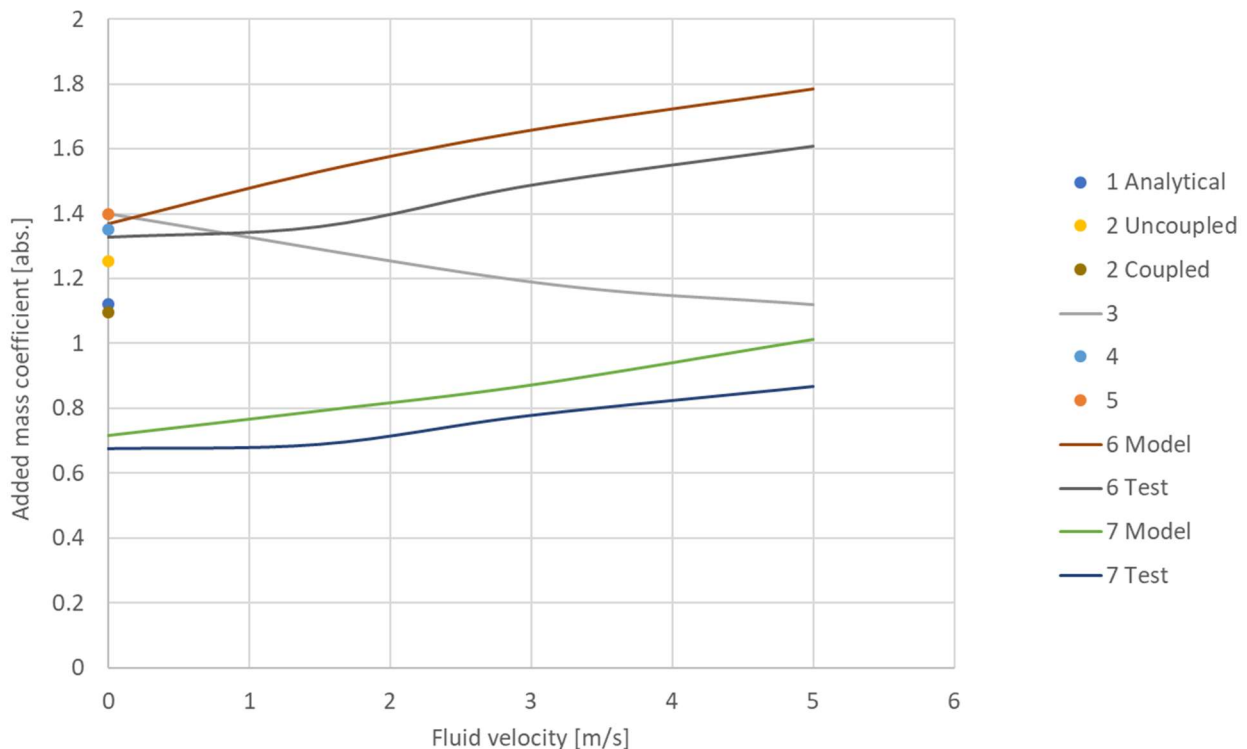
Figure 18: Values for added mass coefficients in 1: Water displacement, 2: (Rigaudeau, et al., 1993), 3: (Pisapia, et al., 2003), 4: (Viallet & Kestens, 2003), 5: (Collard, 2004), 6: (Ricciardi & Boccaccio, 2015), 7: (Ricciardi, 2016)
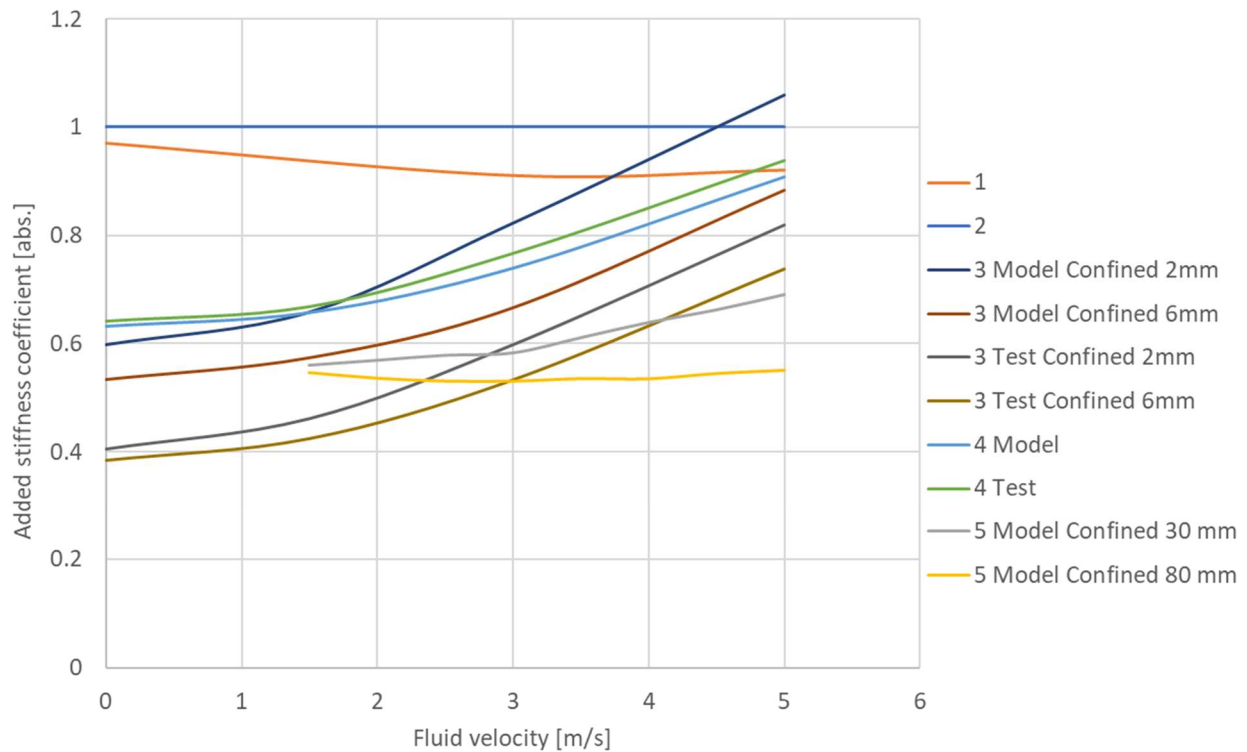
Figure 19: Values for added stiffness coefficients in 1: (Pisapia, et al., 2003), 2: (Collard, 2004), 3: (Ricciardi & Boccaccio, 2015), 4: (Ricciardi, 2016), 5: (Ricciardi, 2017)
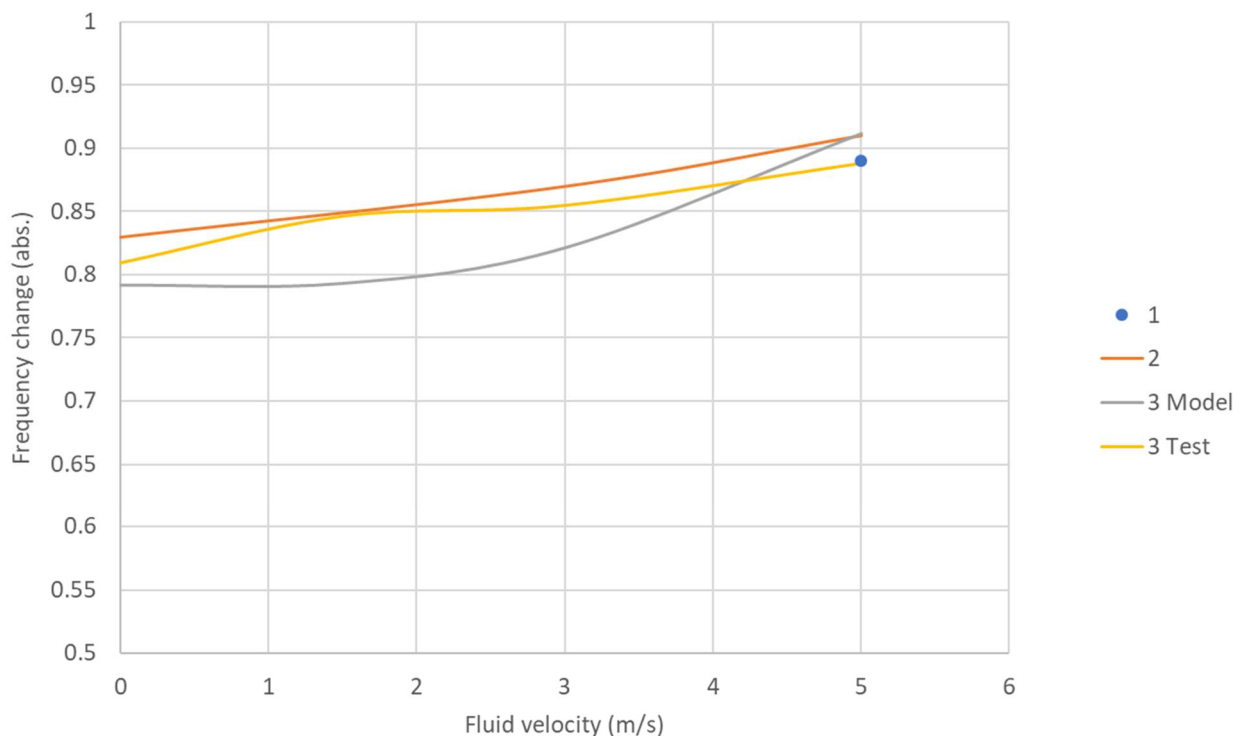
Figure 20: Values for the relationship of natural frequency between still/flowing water and air in 1: (Sunder, 1985), 2: (Pisapia, et al., 2003) and 3: (Ricciardi, 2016)

Based on the beforementioned data, three kinds of fuel assemblies are available to be used in the model (Table 2). The first one represents conventional fuel assembly types regardless of time in the core. For the stiffness, the approximate value measured for moderate deflections up to 4 mm is chosen. The second and third kind represent modern fuel assembly types with a significant decrease in lateral stiffness.

For validation of the fuel assembly lateral stiffness, modal analyses of the first two oscillation modes have been performed (Table 2) and compared to literature values, where FA natural frequencies were determined during operation using neutron flux measurements (Table 3). The calculated values match well with corresponding literature data.

Table 2: Lateral stiffness and calculated natural frequencies according to FA type and state

FA type	Lateral stiffness (N/mm)	1st (Hz)	2nd (Hz)
Type 1	150	3.0	11.5
Type 2 fresh state	60	1.9	7.6
Type 2 aged state	30	1.4	5.6

Table 3: Literature values for the FA natural frequencies (FA supported on each end) determined during operation using neutron flux measurements

Source	Type	BOL/EOL	1st (Hz)	2nd (Hz)
(Fry, et al., 1984)	Westinghouse 4-Loop		3.0-4.0	
	CE 2-Loop		2.3	4.6
	Westinghouse 3-Loop		3.5	
	Framatome CP1		3.2	6.0
	Framatome CP0		3.2	7.4
	KWU 3-Loop		1.8/5.0	11.2/17.5
	3 Loop		2.8	6.6
(Runkel, 1987)		BOL	5.8-6.4	11.0-12.0
(Wach & Sunder, 1988)			3.6-4.0	7.4-8.0
(Bauernfeind, 1988)			3.8	7.6
(Trenty, 1995)	Framatome CP1		2.0-5.0	5.0-7.0
(Fiedler, 2002)	KWU 350 MW		5.8-6.4	11.0-12.0
	KWU 600 MW		4.5	11.2
	KWU Pre-Konvoi		2.6-3.5	6.0-7.0
	KWU Konvoi		2.0-3.0	6.0-7.0
	OPR-1000		2.5-3.0	5.0-6.3
	Framatome CP1		3.0	7.0
(Fontaine & Politopoulos, 2000)			2.8-3.8	
(Viallet & Kestens, 2003)		BOL	2.5	
		EOL	1.4	
(Billerey, 2005)		BOL	3.5	7.1
		EOL	1.8	3.8
(Pohlus & Paquée, 2018)			1.5	3.0

Damping of fuel assembly oscillations comes from fluidic and mechanical phenomena. For moderate damping values D, the maximum response frequency f_{max} to a forced excitation is close to the natural frequency of the undamped system f_0 (Corves, 2010) and the beforementioned considerations maintain their validity.

$$f_{max} = f_0 \sqrt{1 - 2D^2}$$

(3)

Mechanical damping phenomena predominantly include material damping, damping due to the screwing as well as frictional damping. Collisions of fuel assemblies may further involve some degree of squeeze-film damping (Pettigrew, et al., 1998). A survey on available data on mechanical damping (Figure 21), which were measured in context of seismic analyses, revealed a strong dependency on deflection amplitude. Material damping and damping due to the screwing contribute only very little to the overall value, while the majority comes from the hysteresis in deflection (Viallet & Kestens, 2003), (Collard, 2004). As mentioned before, this hysteresis may vanish with the time in the core. Assuming further that the amplitudes in the here investigated application cases are expected comparably small, the structural damping of the fuel assembly may be either neglected or assumed with a small value.
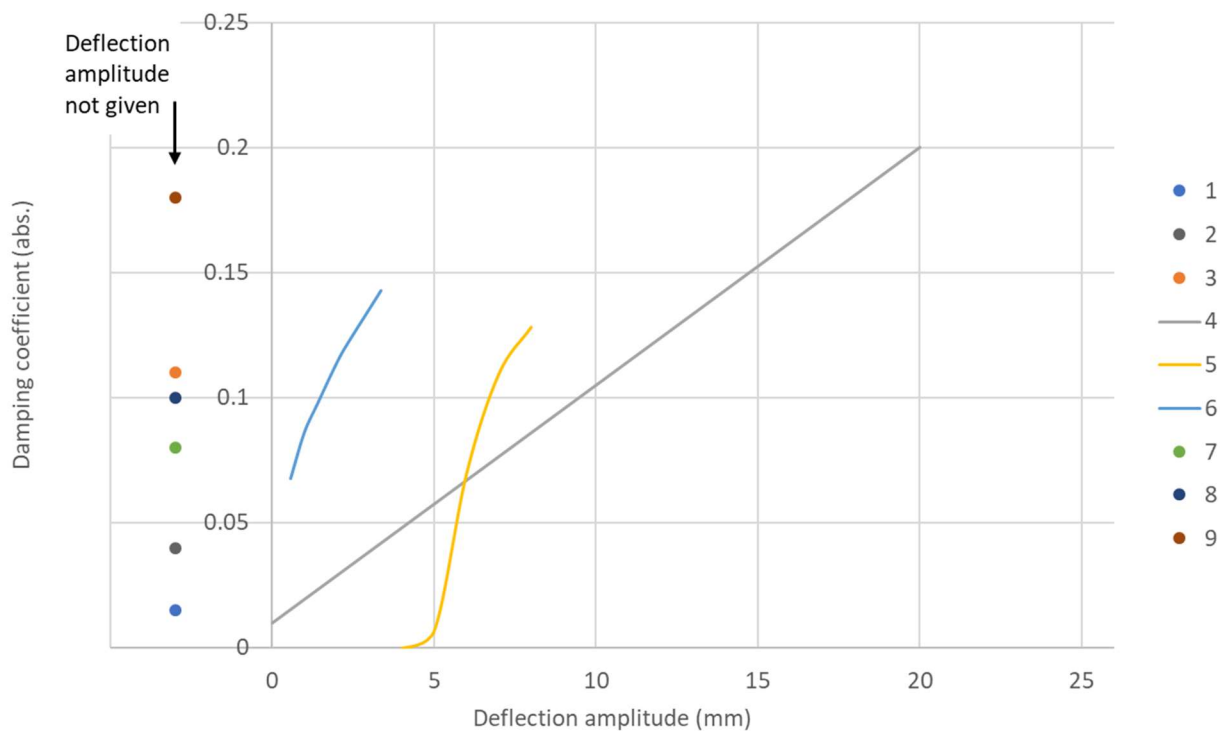
Figure 21: Values for FA mechanical damping in 1/2: (Pettigrew, et al., 1998), 3: (Viallet, et al., 2003), 4: (Viallet & Kestens, 2003), 5: (Pisapia, et al., 2003), 6/7/8/9: (Lu & Seel, 2006), values without given dependency on displacement amplitude are noted left of the Y-axis

The main components of fluidic damping are viscous damping of the surrounding fluid and flow-dependent damping. While the first one is caused by drag effects and can be observed in still fluid, the latter arises from a lift phenomenon due to axial flow velocity relatively to the assembly lateral velocity (Viallet & Kestens, 2003). The phenomena are intensively discussed in (Shah, et al., 2001), (Viallet & Kestens, 2003), (Witters, 2004), (Collard, 2004) and (Lu & Seel, 2006).

Data on fluidic damping, which has been obtained from shaker table tests and corresponding calculations, which were performed in conjunction with seismic analysis, is shown in Figure 22. While the increase with fluid velocity can be observed similar between publications, the general level of damping differs. An interpretation could be that the velocity-independent part may be influenced by boundary conditions, e.g. the width of the channel around the fuel assembly, the test amplitude or the test frequency. As an average value, a damping of D = 0.5 could be assumed for a flow velocity of 5 m/s. As discussed in 3.2.1, this value is only valid for similar excitation types and boundary conditions as in the shaker table experiments, especially with relative lateral motion between fluid and structure.
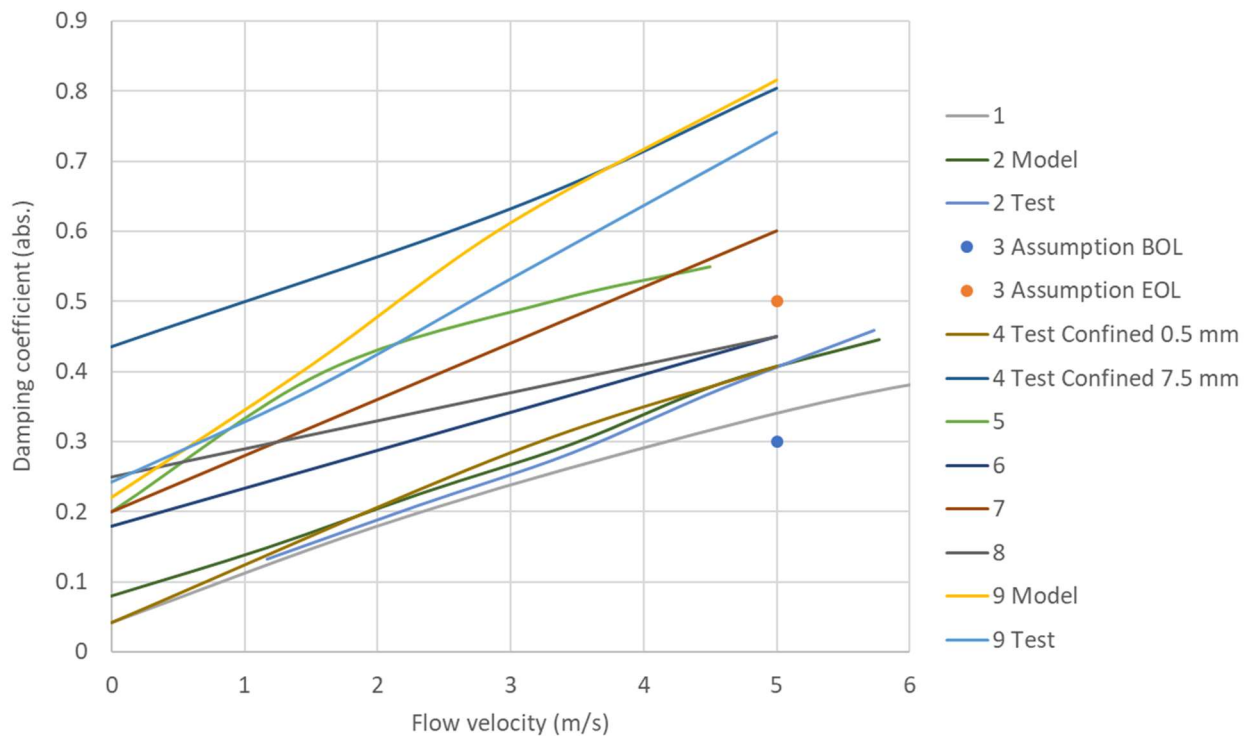
Figure 22: Values for the fluidic damping in 1: (Fujita, 1990), 2: (Shah, et al., 2001), 3: (Viallet & Kestens, 2003), 4: (Pisapia, et al., 2003), 5/6/7/8: (Lu & Seel, 2006), 9: (Ricciardi, 2016)

3.2.3 Model of the system of mechanically coupled components

The model of the system of internals encompasses RPV, core barrel and fuel assemblies. Internals with minor effect, like grid plate or secondary core support, are not included. To simplify the model, the number of fuel assemblies is reduced to only one row of 15 fuel assemblies (Figure 23). To keep the coupling characteristics and the momentum exchange with the core barrel and the RPV realistic, the weight of all 193 fuel assemblies is distributed over the single row. Other fuel assembly parameters are adapted to compensate for the additional weight, keeping the dynamic behavior the same. The underlying assumption of this simplification is that the motions are either uncorrelated, and in this case one row is representative enough for the whole core, or the motions are correlated, and in this case the correlated motion is approximately symmetric in one direction.
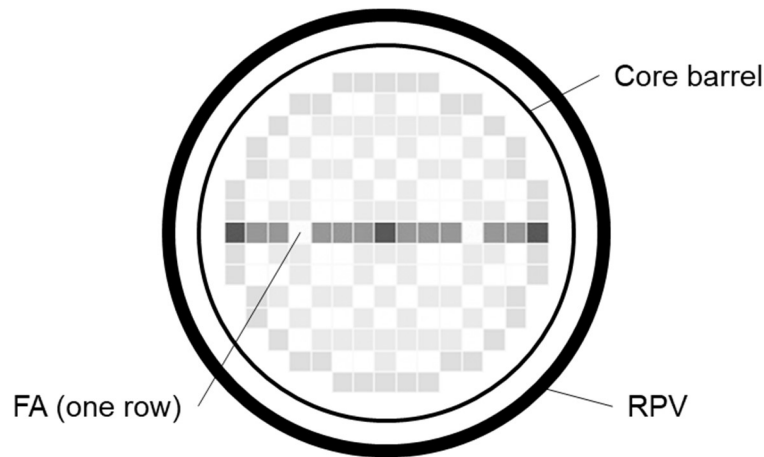
Figure 23: Components that are represented in the mechanical model

The structure of the model is based on the work from (Bauernfeind, 1977) (Figure 13). RPV and core barrel are represented as stiff beams, mounted pivoted to a fixed structure (Figure 24). The structural weight is homogeneously distributed over the beams. At the bottom of the core barrel, an additional point mass is attached, representing the mass of additional structural parts. In a first approximation, the weight of the water content is added to the structure. The water displacement of the core barrel motion within the RPV is considered by further adding the weight of the displaced water to the core barrel in a first approach. This presupposes that the motion of the RPV relative to the environment is small compared to the relative motion between core barrel and RPV (see section 3.2.4).

The fixation of the RPV to the wall of the reactor cavity and the stiffness from the attached primary loops are represented by a spring element, neglecting the damping in this connection. The mounting of the core barrel to the RPV as well as the FSI in the annular gap is modelled by a further combined spring and damper element. The beams representing the RPV and core barrel are discretized into 20 finite elements. The row of 15 fuel assemblies with characteristics according to section 3.2.2 is attached to the core barrel with an axial offset from the core barrel bottom. To include near-field fluidic coupling between adjacent fuel assemblies, further spring elements are included into the model.

The torsion spring stiffness c_{RPV}, the spring stiffness k_{cb} and the damping D_{cb} are determined based on the preliminary work of (Bauernfeind, 1977), (Wach & Sunder, 1977) and (Bauernfeind, 1988) as well as considerations regarding FSI in the annular gap in (Altstadt & Weiss, 1999), (Snyder, 2004) and (Yun Je, et al., 2017).
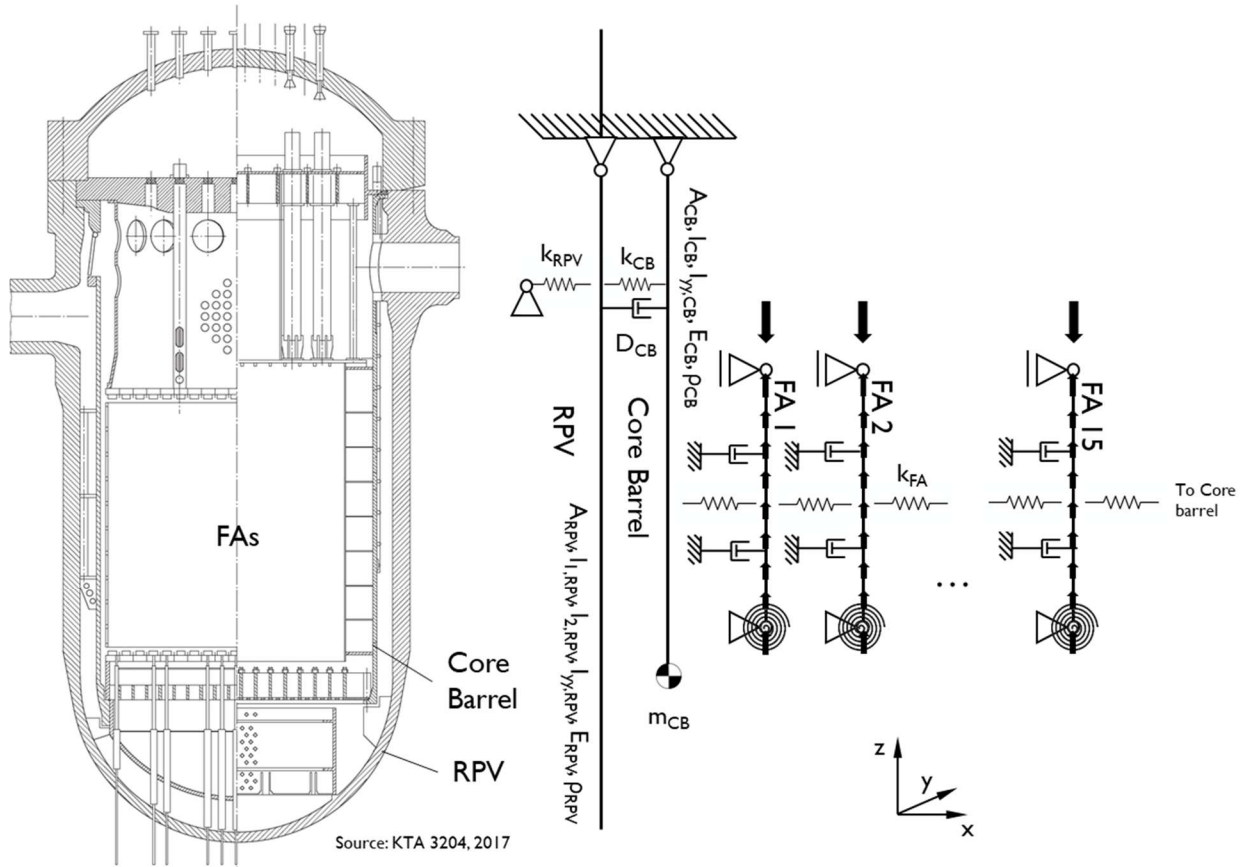
Figure 24: GRS-model of the coupled system of RPV internals

In the reactor situation, the fuel assemblies are coupled among each other via fluidic and mechanical mechanisms. The fluidic coupling comprises inertial and dissipative effects that change the surrounding pressure and velocity field near the oscillator. A far field coupling, which is not included in the model, may further arise e.g. from the redirection of the fixed mass flow over different channels with different flow cross sections. Literature data conclude that the fluidic coupling is either negligible (Fry, et al., 1984), (Rigaudeau, et al., 1993) or very moderate (Broc, et al., 2003), (Witters, 2004), (Ricciardi, et al., 2009). In a calculation from (Witters, 2004), the force on neighboring fuel assemblies in the line of motion accounts for approximately one third of the force acting reactively on the originally moved fuel assembly. (Rigaudeau, et al., 1993) concluded that an indirect fluidic coupling exists via the core baffles. Although not enough quantitative data is available to assume a specific value, the coupling effect could be investigated by a parametric study. It may become especially significant, when the stiffness reaches the magnitude of the fuel assembly stiffness.

The mechanical coupling encompasses the bearing of the components to each other as well as collisions and contact among fuel assemblies and to the core baffle. The latter will get especially relevant, when the motion of the fuel assemblies exceed the width of the gap of approximately 1.6 mm (Seidel, et al., 2015). Collisions and contacts will introduce a strong non-linearity into the system. The consideration of these effects is therefore postponed to future work.

3.2.4 Test calculation with the model of the coupled system of RPV internals on the basic dynamic characteristics

To obtain a first impression of the basic dynamic characteristics of the model described in 3.2.3, a test configuration has been set up with a core consisting of fuel assemblies of Type A, Type B in fresh state and Type B in aged state in equal parts. To obtain a long-term oscillation characteristic with a single energy input, damping has been neglected besides a very small damping for numerical reasons. Furthermore, no coupling among fuel assemblies is assumed (Table 4). The simulation is preceded by a sufficiently long time-interval for settling of oscillations evoked by the hold-down-forces. As an exemplary test excitation, a global lateral acceleration of 0.1 m/s² was applied in a step-function to provide energy to the system.

Table 4: Test configuration of the model

Parameter	Value
Core loading	5x Type A, 5x Type B fresh state, 5x Type B aged state
FA damping	none
FA coupling	none
Excitation	0.1 m/s² global lateral acceleration (step function at t = 0 s)

Figure 25 shows the lateral deflection of the components at an exemplary time step with deformations elevated by a factor 200 in the visualization. Due to the differences in stiffness, the lateral deflection is highest for the aged fuel assemblies of type B followed by the stiffer fuel assemblies of type B in fresh state and type A. In this case no contact between FA takes place because the highest deflection is smaller than the typical FA distance. The deflection of the core barrel and the RPV is much smaller (see also Figure 26).
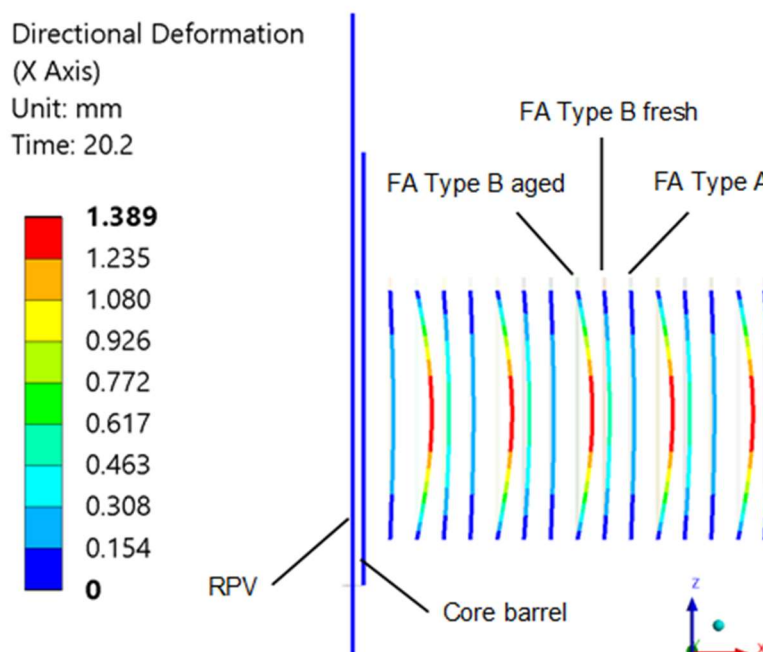
Figure 25: Visualization of the component lateral deflection in an exemplary time step, in the finite element structure code ANSYS Mechanical (deformations elevated by a factor 200)

An interesting aspect can be observed in the course of the lateral deflection of the core barrel bottom (Figure 26). Due to the interaction with the oscillating fuel assemblies, the core barrel shows a non-harmonic broad-banded motion behavior. Although this result is obtained for a specific test configuration, it shows that apart from individual component oscillations, complex core-wide oscillations could arise within the system of coupled oscillators.
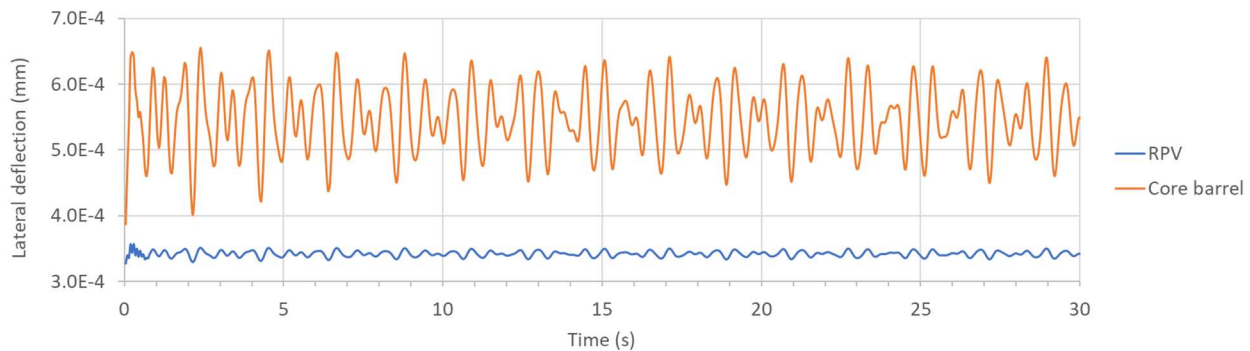
Figure 26: Lateral deflection of the RPV and core barrel bottom after application of test excitation

3.3 Enhanced ATHLET version of the flow through the reactor core

The thermal-hydraulic system code ATHLET (Analysis of THermal-hydraulics of LEaks and Transients) is being developed by GRS for the analysis of the whole spectrum of leaks and transients in different reactors types (Lerchl, et al., 2019). It can be used to simulate the flow conditions inside the core of a reactor. It is also possible to couple it with three-dimensional neutron simulation codes (Langenbuch & Velkov, 2005), (Perin, et al., 2012) to simulate the feedback relations between the fluid conditions (temperature, density) and the neutron physics (power production, neutron flux).

The standard version of ATHLET is not capable to simulate the response of the fluid to time dependent changes in the geometry. Such geometry changes might be the free area within the fuel assemblies and the distance between fuel assemblies. Therefore, an enhanced version of ATHLET has been developed by GRS, which allows to modify the geometry of the thermo fluid elements in a time dependent way and to determine the response to these changes.

3.3.1 Enhanced version of ATHLET to consider FSI-effects

The enhanced version of ATHLET allows to modify the cross-sectional area of each control volume of the thermo fluid elements of ATHLET and the cross-sectional area of so-called junctions, connecting these control volumes. It is also possible to change the hydraulic diameter. Additionally, it is necessary to modify the geometry factor for friction losses to reflect the changes in the cross-sectional area and the hydraulic diameter.

Changes in the cross-sectional area of the thermo fluid elements are not considered in the equations solved by ATHLET. Therefore, the effect on the mass and energy stored within one control volume must be considered by adding explicit mass and energy source or sink terms to the fundamental equations. These terms were added to ATHLET analogously to the implementation of the mass and energy source terms for the oxidation of Zirconium of the fuel rod claddings (Austregesilo, et al., 2019).

Changes of the cross-sectional area of a fuel assembly lead to changes of the mass flow rate and its enthalpy. This is modelled using sink and source terms for the mass flow and enthalpy in the control volumes describing the fuel assembly. If the cross-sectional area is increased, mass and energy sink will take up the additional mass and energy in the control volumes. If the cross-sectional area is decreased, mass and energy sources represent the mass and enthalpy squeezed out. Summing over the whole reactor core mass and energy sinks and sources cancel out each other. In the current implementation it is assumed that the fluid is only in liquid state. So, no changes are applied to the equations for the vapor state and for non-condensable gases.

The enhancements are implemented using the so-called controller infrastructure of ATHLET, which allow to call ATHLET methods from a Python script (Kommajosyula & Xiao, 2014), (Scheuer, 2019), (Herb, 2019). ATHLET is linked as a shared library which can be loaded and called from a Python program.

A Python wrapper script is controlling the simulation. It determines the time steps, does the FSI calculations, modifies the internal data of ATHLET and calls ATHLET to do the thermal hydraulic calculations for a given time step.

The FSI related calculations are done in the Python script calculating the cross-sectional area (CSA) of each fuel assembly depending on the simulation time and the values of the mass and energy source terms. For a given time step, these values are recalculated and written into the program memory of ATHLET. The library libfde is used to access the internal memory of ATHLET. This library represents the ATHLET memory as a so-called hash map, so that the selected internal module variables of ATHLET can be accessed by its names. The ATHLET code within the shared library is called to do the thermal hydraulic calculations. After ATHLET has performed the simulation up to the given time value, the values of interest for the FSI simulation are extracted from ATHLET and written into files so they can be analyzed by post-processing tools, e.g. the pressure differences between the fuel assemblies or the resulting fluid dynamic forces on the fuel assemblies.

3.3.2   ATHLET model used with enhanced ATHLET version

The ATHLET model for the simulations of FSI effects developed by GRS is based on a 193 core-channel-model. Its ground view is shown in Figure 27. The model contains two branch objects, one at the bottom and one at the top, which are connected by the 193 core channels and an additional by-pass thermo fluid object. Figure 28 shows the side view of the model with the nodalization of two of the 193 core channels, the cross connections between them, the by-pass channel, the lower and the upper plenum.

Figure 29 schematically shows the area assigned to a fuel assembly in the ATHLET model. The white circles in the middle represent the area occupied by the 236 fuel rods and the 20 control rod guide tubes. The red area shows the flow area within the fuel assembly, which is assumed to be constant. The blue area in Figure 29 represents the area of the gap between the fuel assemblies. This distance between fuel assemblies at rest in a German pre-KONVOI reactor is 1.6 mm (see also section 2.2). If the fuel assemblies are at their idle position, half of the 1.6 mm are assigned to each of the two adjacent fuel assemblies. Four gap size values are assigned to each fuel assembly, one for each direction (north, east, south, west).

If the fuel assemblies are deviated from the idle position, the gap size must be greater than zero. The upper limit is given by the fact, that the sum of the gap sizes in one direction for a row or a

column of fuel assemblies must be equal to the number of fuel assemblies in this row/column multiplied by 1.6 mm.
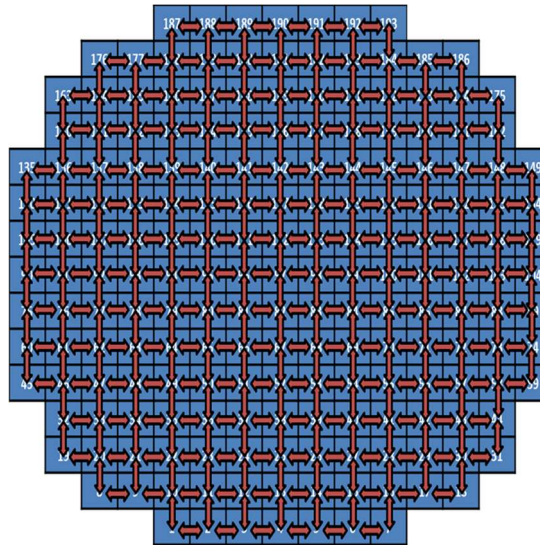
Figure 27: 193-channel ATHLET core model (ground view)
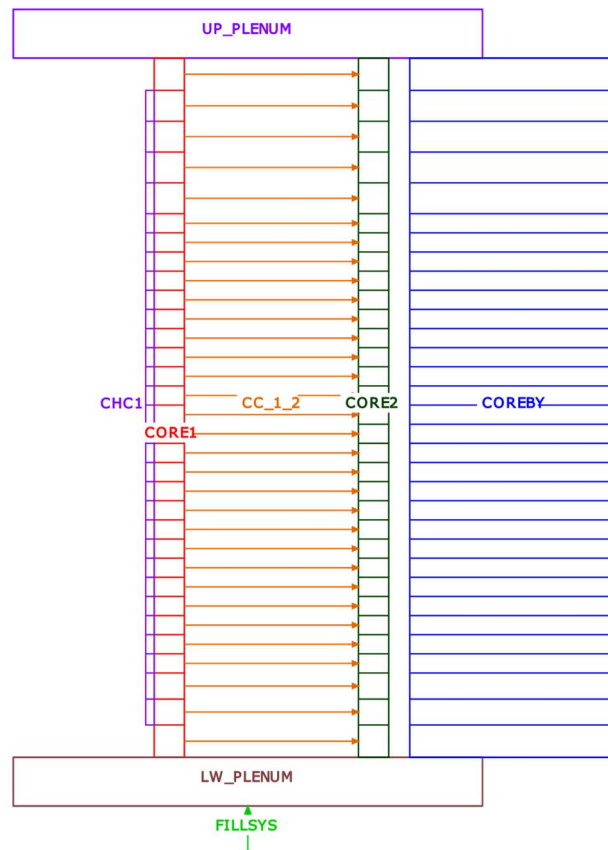
Figure 28: 193-channel ATHLET core model (side view) with two core channels (CORE1, CORE2), the cross connections between them (CC_1_2), core by-pass (COREBY), the lower (LW_PLENUM) and the upper (UP_PLENUM) branches
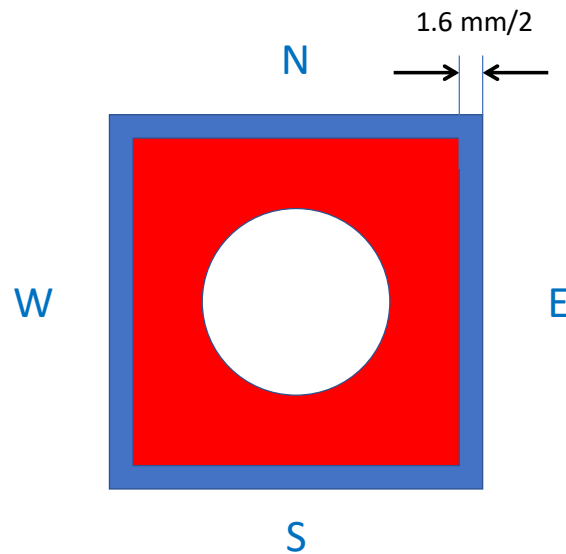
Figure 29: Schematic geometry of one fuel assembly (white circle: area occupied by fuel rods and guide tubes, red: cross section flow area of the fuel assembly, blue: area of gaps between fuel assemblies)

3.3.3 Test calculation using the enhanced ATHLET version

A test calculation with the 193-core-channel model was performed. After a quiet period of 5 s, the cross-sectional areas for the fuel assemblies were changed in an oscillating way with a frequency of 1 Hz.

In axial direction (bottom to top in Figure 28) the positions of the fuel assemblies were modified with a sine-shaped form. So, the position change in the middle was the largest and at bottom and top it was zero.

For the plane in the middle of the core in axial direction the first fuel assemblies were moved to the left, so that after 0.25 s all fuel assemblies in each row except for the most left one had a gap size of zero at the east and west position. The east and west gap size of the left most fuel assembly was set to a value (both the same value) so their sum corresponds to the total gap size of that column. After 0.5 s the fuel assemblies were back to their idle position, after 0.75 s all but the right most fuel assembly had east and west gap size zero and after 1.0 s all fuel assemblies were back in their idle position (see Figure 30). The corresponding time dependent horizontal position changes (in east-west direction) of the two fuel assemblies 90 and 104 (the left- and rightmost fuel assemblies in the center row) are shown in Figure 31.

These changes of the cross-sectional areas of the fuel assemblies result in pressure differences (Figure 32) between adjacent fuel assemblies and a change of the fluid speed (Figure 33).
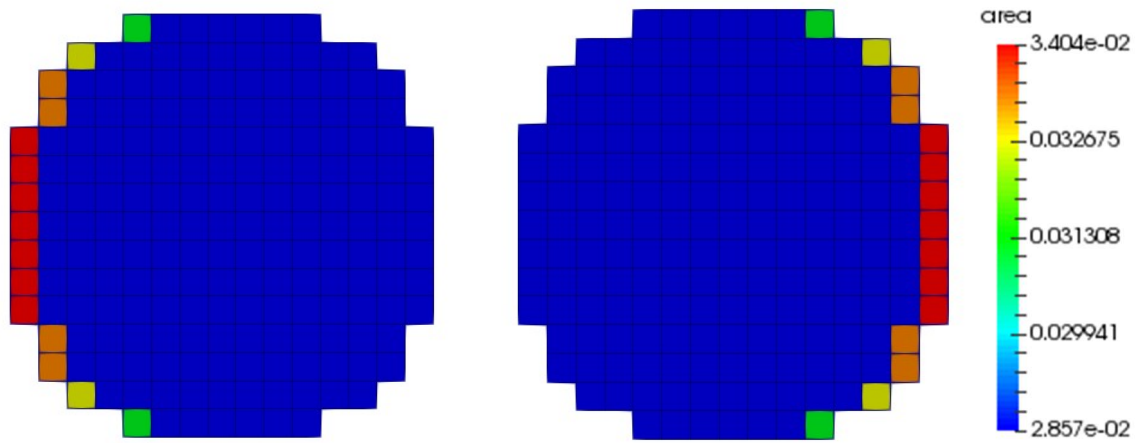
**Figure 30: Maximal/minimal cross-sectional areas of fuel assemblies in the axial middle of the core
(t = 5.24 s (left), t = 5.74 s (right))**
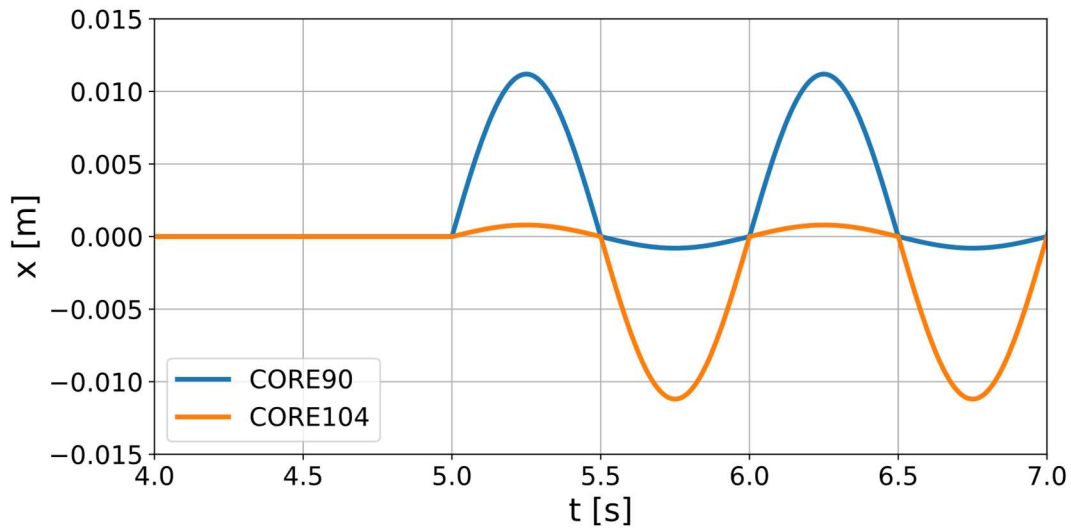
Figure 31: Horizontal position change of fuel assemblies 90 and 104
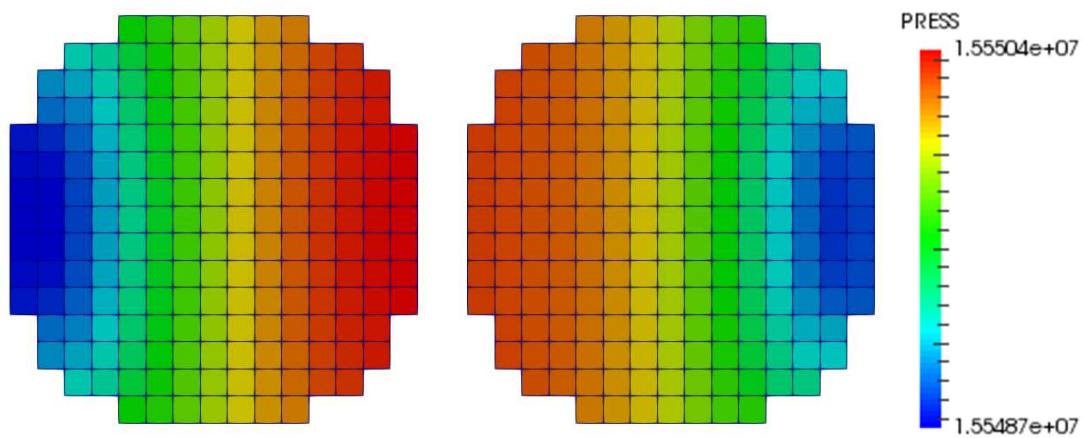
**Figure 32: Pressure in the axial middle of the core
(t = 5.14 s (left), t = 5.69 s (right))**
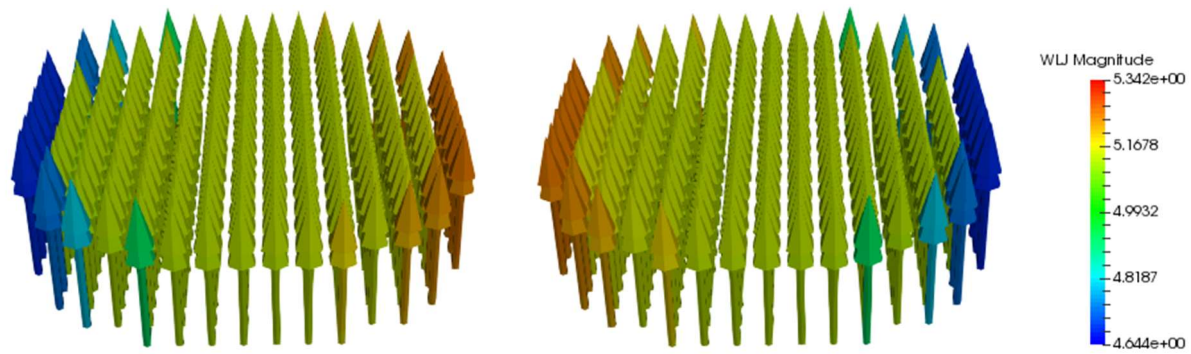
**Figure 33: Coolant velocities in the axial middle of the core
(t = 6.24 s (left), t = 6.74 s (right))**

By integrating the pressure differences between two core channels over the area connecting them, i.e. the side length of the fuel channel times the height, a fluid dynamic force on each fuel assembly can be calculated. Also, the force created by the stagnation pressure on the fuel assembly by the flow in the cross connections are integrated. For comparison, an elastic force is calculated by the deformation of the fuel rod assuming an elastic module of 20 N/mm. The resulting forces on five fuel assemblies in the center row are shown in Figure 34.

The force by the stagnation pressure seems negligible compared to the other two for all fuel assemblies. The other two forces are of the same order of magnitude.

3.3.4   Possible additional multi-physics couplings

It has been found that the changes in the fuel assembly areas and the corresponding changes of the fuel velocities also result in time dependent changes of the fluid temperature, as shown in Figure 35. The test calculation was performed with a thermal core power of 1.1 GW resulting in a temperature increase of 10 K over the height of the core. The time dependent temperature changes at the axial middle of the core were about 0.3 K and in the upper control volumes of about 1 K.

In (Herb, 2019) it was found that depending on the frequency, a temperature change of 1 K can result in power and neutron flux changes in the order of 10 % of the reactor power. Therefore, in future simulations ATHLET will be coupled with a three-dimensional neutronics code to calculate the feedback of these temperature changes on the local power production and correspondingly to the local neutron flux amplitude.
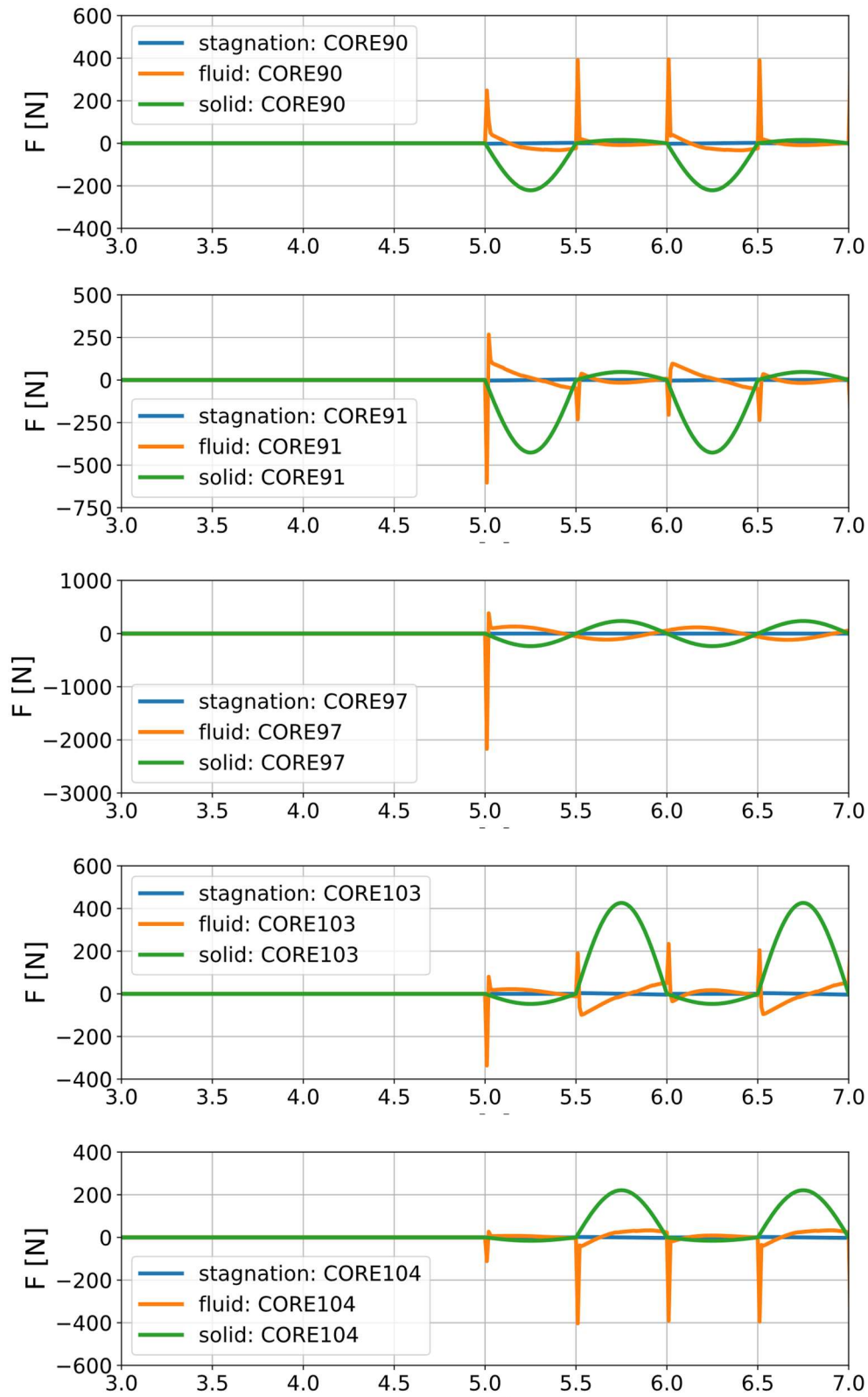
Figure 34: FSI-forces on the fuel assemblies 90, 91, 97, 103, 104 (all in the central row)
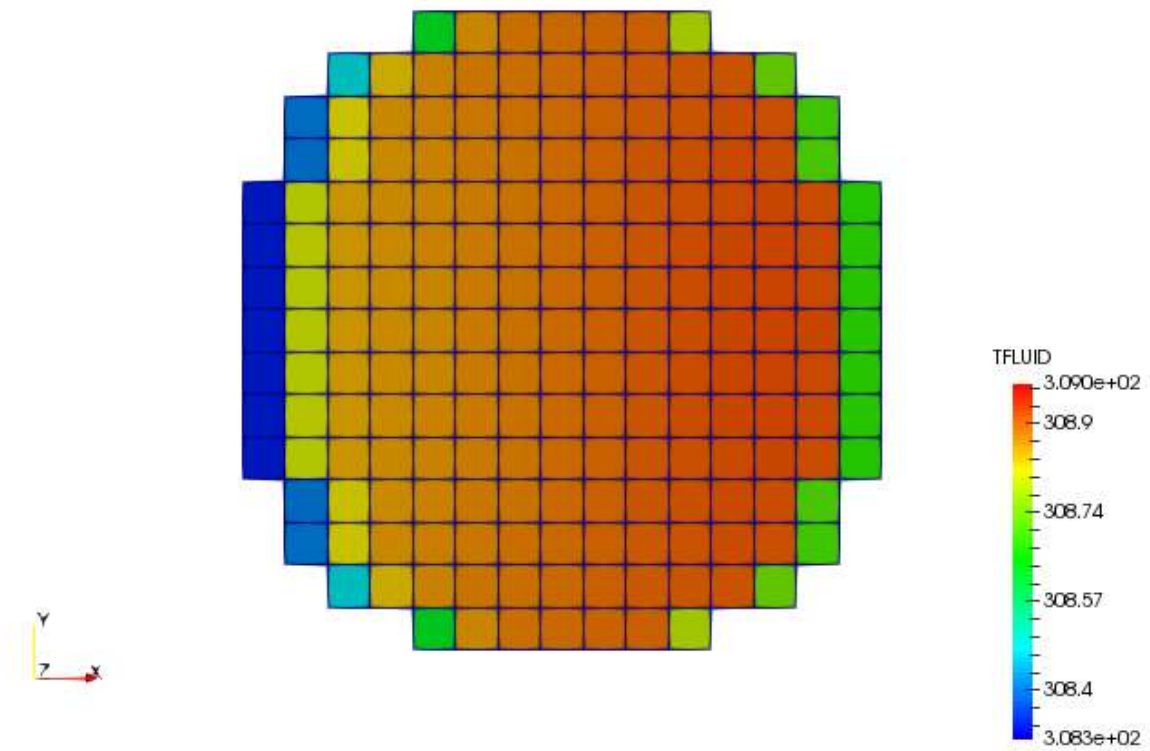
Figure 35: Fluid temperature (°C) in the upper control volumes of the core channels at time 14.64 s

4 Reduced order modelling of the core internals dynamic behavior

Model order reduction techniques are mathematical methods to reduce the dimension of a dynamical system. They are employed in order to lower the computational cost of a numerical simulation both in terms of memory and processing speed. These methods are used in many disciplines ranging from electrical engineering over biological systems to fluid mechanics (Benner, et al., 2013), (Baur, et al., 2014), (Bai, 2002). In reactor physics, they were already applied, for example, to the modelling of thermal hydraulics (see (Manthey, et al., 2017), (Prill & Class, 2014)).

Mathematically speaking, model order reduction is a prescription on how to transform a dynamical system (which will be called full order model – FOM in the following) of the form

$$\frac{\mathrm{d}\mathbf{x}(t)}{\mathrm{d}t} = \boldsymbol{F}(\mathbf{x}(t), t) \tag{4}$$

to a reduced order system

$$\frac{\mathrm{d}\tilde{\mathbf{x}}(t)}{\mathrm{d}t} = \widetilde{\boldsymbol{F}}(\tilde{\mathbf{x}}(t), t), \tag{5}$$

where $\mathbf{x} \in \mathbb{R}^n$ are the state variables (or the degrees of freedom) of the full order model and $\tilde{\mathbf{x}} \in \mathbb{R}^k$ the state variables of the reduced order model. $\boldsymbol{F}: \mathbb{R}^n \times \mathbb{R} \to \mathbb{R}^n$ and $\widetilde{\boldsymbol{F}}: \mathbb{R}^k \times \mathbb{R} \to \mathbb{R}^k$ are functions which are sufficiently often differentiable. The dimension k is assumed to be smaller than the dimension n of the original system in order to obtain a reduced system. (We only consider ordinary differential equations here, since the ANSYS Mechanical model provided in subtask 1.1.1 is a large ODE model after the application of FEM). The system in Eq. (5) is thought of as a small dimensional representation of the full order model in Eq. (4).

The various methods differ in their approach on how the reduction of the system is ultimately achieved. Naturally, some information is lost in the reduction process and the distinguishing property of the methods is which information is retained.

For this report, TU Dresden has considered only projection-based model order reduction techniques. These techniques use two linear transformations $\mathbf{W} \in \mathbb{R}^{n \times k}$ and $\mathbf{V} \in \mathbb{R}^{n \times k}$ with $\mathbf{W}^{\mathrm{T}}\mathbf{V} = \mathbf{id}_{k \times k}$, in order to transform the FOM into the ROM. The columns of $\mathbf{V}$ span the subspace of states modelled by the ROM, i.e. a ROM state is represented by a linear combination of the columns of $\mathbf{V}$ in the original state space:

$$\mathbf{x} = \mathbf{V}\widetilde{\mathbf{x}}. \tag{6}$$

The columns of $\mathbf{V}$ will henceforth be called modes. The columns of $\mathbf{W}$ represent vectors of weights. The FOM equation is transformed to the ROM equation by imposing that the weighted sum of the residual of all weights in $\mathbf{W}$ vanishes for the states spanned by $\mathbf{V}$:

$$0 = \mathbf{W}^T \left(\frac{\mathrm{d}\big(\mathbf{V}\tilde{\mathbf{x}}(t)\big)}{\mathrm{d}t} - \boldsymbol{F}(\mathbf{V}\tilde{\mathbf{x}}(t), t) \right). \tag{7}$$

It is clear from Eq. (7) that with the definition of $\widetilde{\boldsymbol{F}}(\tilde{\mathbf{x}}, t)$

$$\widetilde{\boldsymbol{F}}(\tilde{\mathbf{x}}, t) := \mathbf{W}^{\mathrm{T}} \boldsymbol{F}(\mathbf{V}\tilde{\mathbf{x}}, t). \tag{8}$$

We then obtain the differential equation of the ROM. In mathematical terms, the different model order reduction techniques presented in this report differ in the procedure on how to obtain $\mathbf{W}$ and $\mathbf{V}$ from the original system.

A special case of interest for this report is the case where the dynamical system is linear, that is, of the form

$$\begin{cases} \dfrac{\mathrm{d}\mathbf{x}(t)}{\mathrm{d}t} = \mathbf{A}\,\mathbf{x}(t) + \mathbf{B}\,\mathbf{u}(t) \\ \boldsymbol{y}(t) = \mathbf{L}^{\mathrm{T}}\,\mathbf{x}(t). \end{cases} \tag{9}$$

This form of a dynamical system with a state vector $\mathbf{x}(t) \in \mathbb{R}^{\mathrm{n}}$, a system matrix $\mathbf{A} \in \mathbb{R}^{\mathrm{n} \times \mathrm{n}}$, an input vector $\mathbf{u}(t) \in \mathbb{R}^{\mathrm{m}}$ and additionally an output vector $\mathbf{y}(t) \in \mathbb{R}^{\mathrm{p}}$, is common in linear control theory. It incorporates the notion that the exact state $\mathbf{x}(t)$ of a system is, in general, not known to an observer, but that only a few output quantities $\mathbf{y}(t)$ may be accessible.

In this case, the transformations with $\mathbf{W}$ and $\mathbf{V}$ convert the system into

$$\begin{cases} \dfrac{\mathrm{d}\tilde{\mathbf{x}}(t)}{\mathrm{d}t} = \widetilde{\mathbf{A}}\,\tilde{\mathbf{x}}(t) + \widetilde{\mathbf{B}}\,\mathbf{u}(t) \\ \boldsymbol{y}(t) = \tilde{\mathbf{L}}^{\mathrm{T}}\,\tilde{\mathbf{x}}(t), \end{cases} \tag{10}$$

with

$$\widetilde{\mathbf{A}} = \mathbf{W}^{\mathrm{T}}\,\mathbf{A}\,\mathbf{V}, \tag{11}$$
$$\widetilde{\mathbf{B}} = \mathbf{W}^{\mathrm{T}}\,\mathbf{B}, \tag{12}$$
$$\tilde{\mathbf{L}} = \mathbf{V}^{\mathrm{T}}\mathbf{L}. \tag{13}$$

Thus, with projection-based model order reduction a linear dynamical system is transformed to another linear dynamical system of lower order with the matrix transformations given above.

4.1 Model order reduction techniques

In this section, three model order reduction techniques applicable to the model are described in mathematical detail. These are proper orthogonal decomposition (POD), Krylov subspace methods and Gramian based methods.

4.1.1 Proper orthogonal decomposition

Proper orthogonal decomposition (POD) is a method were the weights $\mathbf{W}$ and modes $\mathbf{V}$ are generated from actual time series data (Lenaerts, et al., 2001), (Rega & Troger, 2005), (Glösmann & Kreuzer, 2005). To this end, a transient is either simulated or generated by experiment. This transient is sampled at a series of discrete points in time $t_i, i = 1, \dots, N$ and the state variable $\mathbf{x}_i := \mathbf{x}(t_i)$ sampled at t_i is written into the i-th column of the so-called snapshot matrix $\mathbf{Y} \in \mathbb{R}^{n \times N}$ (i.e. $y_{ji} = x_j(t_i)$).

Then a mathematical method called singular value decomposition (SVD) is used to decompose the snapshot matrix $\mathbf{Y}$ into a matrix product of two orthogonal (or unitary) matrices $\widehat{\mathbf{V}} \in \mathbb{R}^{n \times n}$ and $\mathbf{U} \in \mathbb{R}^{N \times N}$, and a matrix $\mathbf{\Sigma} \in \mathbb{R}^{n \times N}$. $\mathbf{\Sigma}$ is zero except for positive elements $\sigma_1 \geq \sigma_2 \geq \cdots \geq \sigma_r > 0$ on its main diagonal for some $r \leq \min\{n, N\}$. Then $\mathbf{Y}$ is of the following form:

$$\mathbf{Y} = \widehat{\mathbf{V}} \, \mathbf{\Sigma} \, \mathbf{U}^{\mathrm{T}}. \tag{14}$$

The matrix product in Eq. (14) can be rewritten in a more instructive form as

$$\mathbf{Y} = \sum_{i=1}^{r} \sigma_i \mathbf{v}_i \mathbf{u}_i^{\mathrm{T}}, \tag{15}$$

where $\mathbf{v}_i \in \mathbb{R}^n$ and $\mathbf{u}_i \in \mathbb{R}^N$ are the i-th column of $\widehat{\mathbf{V}}$ and $\mathbf{U}$, respectively. Consequently, $\mathbf{Y}$ is decomposed into a weighted sum of matrices $\mathbf{K}_i = \mathbf{v}_i \mathbf{u}_i^{\mathrm{T}}$, such that $\mathbf{Y}\mathbf{u}_i = \sigma_i \mathbf{v}_i = \sigma_i \mathbf{K}_i \mathbf{u}_i$. Each of the matrices $\mathbf{K}_i$ can be interpreted as a mode $\mathbf{v_i}$ modulated in time by $\mathbf{u}_i$. It can be shown that if the sum in Eq. (15) is cut at order k this yields an optimal approximation of $\mathbf{Y}$ by at most k matrices of the form $\mathbf{K} = \mathbf{v}\mathbf{u}^{\mathrm{T}}$ in the Frobenius norm. That means that

$$\widetilde{\mathbf{Y}} = \sum_{i=1}^{k} \sigma_i \mathbf{v}_i \mathbf{u}_i^{\mathrm{T}} \tag{16}$$

has the lowest mean squared distance from $\mathbf{Y}$ of all matrices with at most k dimensional image. Therefore, the matrices of weights $\mathbf{W}$ and of the modes $\mathbf{V}$ are both chosen as the first k columns of the matrix $\widehat{\mathbf{V}}$. The idea is that the essential modes of the dynamic are present in the transient and thus identified by the singular value decomposition.

In summary, in order to apply the POD model order reduction technique a time series of the detailed model has to be decomposed by SVD and the mode and weight matrix are chosen as the columns of $\widehat{\mathbf{V}}$ in Eq. (14).

4.1.2 Krylov subspace methods

Krylov subspace methods are a popular form of model order reduction for linear dynamical systems (Bai, 2002), (Antoulas, et al., 2001), (Salimbahrami & Lohmann, 2002). They are based on the so called Krylov subspaces

$$\mathcal{K}_k(\mathbf{A}, \mathbf{x}) := \text{span}\{\mathbf{x}, \mathbf{A}\,\mathbf{x}, \mathbf{A}^2\,\mathbf{x}, \dots, \mathbf{A}^{k-1}\,\mathbf{x}\}, \tag{17}$$

which are widely utilized in order to numerically solve large systems of linear equations. In this section we will only consider linear differential equations of the form:

$$\begin{cases} \dfrac{d\mathbf{x}(t)}{dt} = \mathbf{A}\,\mathbf{x}(t) + \mathbf{B}\,\mathbf{u}(t) \\ \mathbf{y}(t) = \mathbf{L}^{\mathrm{T}}\,\mathbf{x}(t). \end{cases} \tag{18}$$

Equation (8) can be transformed into the frequency space via a Laplace transform to

$$\hat{\mathbf{y}}(s) = \mathbf{L}^{\mathrm{T}}\,(s\,\mathbf{id} - \mathbf{A})^{-1}\,\mathbf{B}\,\hat{\mathbf{u}}(s), \tag{19}$$

where we assume that $\mathbf{x}(0) = \mathbf{x}_0 = 0$. The matrix

$$\mathbf{H}(s) := \mathbf{L}^{\mathrm{T}}\,(s\,\mathbf{id} - \mathbf{A})^{-1}\,\mathbf{B} \tag{20}$$

is called transfer matrix of the linear system. It determines the input-output characteristics of a linear dynamical system.

In Krylov subspace model order reduction, the matrices $\mathbf{W}$ and $\mathbf{V}$ are chosen in such a way that the transfer matrix of the ROM approximates the transfer matrix of the original system. Since the response characteristics of the transfer matrix are determined by its poles and roots, Krylov subspace methods use a Padé approximant. This is the "best" approximation of a function by a rational function of a certain order. The Padé approximant $\widetilde{\mathbf{H}}(s)$ of order $[l/q]$ agrees in derivatives with the derivatives of the transfer matrix $\mathbf{H}(s)$ up to order $l + q$ at a selected point s_0:

$$\mathbf{H}^{(r)}(s_0) = \widetilde{\mathbf{H}}^{(r)}(s_0), \qquad \text{for } r \leq l + q. \tag{21}$$

From Eq. (20), it follows that, assuming s_0 is not in the spectrum of $\mathbf{A}$, $\mathbf{H}(s)$ can be expressed as

$$\mathbf{H}(s) = \sum_{r=0}^{\infty}(s - s_0)^r\,\mathbf{L}^{\mathrm{T}}\,\mathbf{G}^r\,\mathbf{R}, \tag{22}$$

with

$$\mathbf{G} := (s - s_0)(s_0\,\mathbf{id} - \mathbf{A})^{-1} \quad \text{and} \quad \mathbf{R} := (s_0\,\mathbf{id} - \mathbf{A})^{-1}\,\mathbf{B}. \tag{23}$$

The expression $\mathbf{L}^{\mathrm{T}} \, \mathbf{G}^r \, \mathbf{R}$ in Eq. (22) is called the r-th moment of the transfer matrix. It can be shown (see [11]) that these moments are matched up to order $2k - 1$ by reducing the transfer matrix by projection onto the Krylov subspaces

$$\mathcal{K}_k(\mathbf{G}, \mathbf{R}) = \mathrm{span}\{\mathbf{R}, \mathbf{G}\,\mathbf{R}, \dots, \mathbf{G}^{k-1}\,\mathbf{R}\} \tag{24}$$

and

$$\mathcal{K}_k(\mathbf{G}^{\mathrm{T}}, \mathbf{L}) = \mathrm{span}\left\{\mathbf{L}, \mathbf{G}^{\mathrm{T}}\,\mathbf{L}, \dots, (\mathbf{G}^{\mathrm{T}})^{k-1}\,\mathbf{L}\right\}. \tag{25}$$

Thus, the columns of the matrices $\mathbf{W}$ and $\mathbf{V}$ are given by a choice of biorthogonal bases, i.e. $\mathbf{W}^{\mathrm{T}}\,\mathbf{V} = \mathbf{id}$, of the two Krylov subspaces $\mathcal{K}_k(\mathbf{G}^{\mathrm{T}}, \mathbf{L})$ and $\mathcal{K}_k(\mathbf{G}, \mathbf{R})$. These are usually found by the application of the Lanczos or the Arnoldi algorithm (Feldmann & Freund, 1995), which are both modified Gram-Schmidt processes.

In summary: Krylov subspace reduction works by finding biorthogonal bases of the Krylov subspaces $\mathcal{K}_k(\mathbf{G}^{\mathrm{T}}, \mathbf{L})$ and $\mathcal{K}_k(\mathbf{G}, \mathbf{R})$ for the weights $\mathbf{W}$ and the modes $\mathbf{V}$ via e.g. the Lanczos algorithm. The transfer matrix of the reduced order system is then the best rational approximation of order [k-1/k] of the transfer matrix of the original system. This allows for a tuning of the desired frequency scope of the model by the choice of the parameter s_0 (it is also possible to choose multiple expansion points) (Baur, et al., 2014).

4.1.3 Balanced truncation

Balanced truncation is a Gramian based method. Gramian based methods are linear model order reduction techniques originating from linear control theory. They thus operate on dynamical systems of the form:

$$\begin{cases} \dfrac{\mathrm{d}\mathbf{x}(t)}{\mathrm{d}t} = \mathbf{A}\,\mathbf{x}(t) + \mathbf{B}\,\mathbf{u}(t) \\ \boldsymbol{y}(t) = \mathbf{L}^{\mathrm{T}}\,\mathbf{x}(t). \end{cases} \tag{26}$$

They rely on the concept of controllability and observability of a linear dynamical system. A linear dynamical system is controllable if there is an input function $\mathbf{u}(t)$ for any pair of an initial state $\mathbf{x}_0$ and end state $\mathbf{x}_{\mathrm{e}}$ such that $\mathbf{x}(t_0) = \mathbf{x}_0$ can be transferred to $\mathbf{x}(t_{\mathrm{e}}) = \mathbf{x}_{\mathrm{e}}$ in the finite amount of time $t_{\mathrm{e}} - t_0$. It can be shown that this question is equivalent to the question of whether $\mathbf{x}_{\mathrm{e}} - \exp(\mathbf{A}(t_{\mathrm{e}} - t_0))\mathbf{x}_0$ is in the space spanned by the columns of the controllability Gramian $\mathbf{W}_{\mathrm{c}}$, which is defined as:

$$\mathbf{W}_{\mathrm{c}} := \int_{t_0}^{t_{\mathrm{e}}} \exp(\mathbf{A}(t_{\mathrm{e}} - t_0))\,\mathbf{B}\,\mathbf{B}^{\mathrm{T}}\,\exp\left(\mathbf{A}^{\mathrm{T}}(t_{\mathrm{e}} - t_0)\right)\,\mathrm{d}t. \tag{27}$$

The system is called observable if the initial state can be reconstructed by the knowledge of the output signal $\mathbf{y}(t)$ in a finite time interval and if the input signal $\mathbf{u}(t)$ is known. This is possible if the observability Gramian of the system

$$\mathbf{W}_o := \int_{t_0}^{t_e} \exp\left(\mathbf{A}^T(t_e - t_0)\right) \mathbf{L}^T \mathbf{L} \exp\left(\mathbf{A}(t_e - t_0)\right) \mathrm{d}t \tag{28}$$

is non-singular.

If the eigenvalues of the system matrix $\mathbf{A}$ have only negative real parts, then both Gramians (for $t_0 = 0$ and $t_e = \infty$) can be uniquely determined by the following matrix equations (continuous Lyapunov equations):

$$\mathbf{A}\mathbf{W}_c + \mathbf{W}_c\mathbf{A}^T = -\mathbf{B}\,\mathbf{B}^T \tag{29}$$

$$\mathbf{A}^T\mathbf{W}_o + \mathbf{W}_o\mathbf{A} = -\mathbf{L}^T\,\mathbf{L}. \tag{30}$$

A dynamical system can have many different equivalent realizations with the same transfer function which may possess different controllability and observability Gramians (Chen, 1998).

The idea of balanced truncation is to first choose a realization of the dynamical system where controllability and observability Gramian are both given by a diagonal matrix $\mathbf{\Sigma} = \mathrm{diag}(\sigma_1, \dots, \sigma_n)$ with $\sigma_1 \geq \sigma_2 \geq \cdots \geq \sigma_n$. Then the system is projected onto its first k components leaving only those states which are most affected by the input and most easily observed.

The following discussion is restricted to the case of a stable system where the eigenvalues of $\mathbf{A}$ have only negative real parts. Then, both Gramians $\mathbf{W}_c$ and $\mathbf{W}_o$ are also positive definite and a Cholesky decomposition can be applied:

$$\mathbf{W}_o = \mathbf{Z}_o\mathbf{Z}_o^T \quad \text{and} \quad \mathbf{W}_c = \mathbf{Z}_c\mathbf{Z}_c^T. \tag{31}$$

This allows a singular value decomposition of the product:

$$\mathbf{Z}_c^T\mathbf{Z}_o = (\mathbf{V}_1 \quad \mathbf{V}_2)\begin{pmatrix} \mathbf{\Sigma}_1 & 0 \\ 0 & \mathbf{\Sigma}_2 \end{pmatrix}\begin{pmatrix} \mathbf{U}_1^T \\ \mathbf{U}_2^T \end{pmatrix}, \tag{32}$$

where the matrices were split in blocks of sizes $k \times k$, $(k-1) \times k$, $k \times (k-1)$ and $(k-1) \times (k-1)$.

The matrices of weights $\mathbf{W}$ and of modes $\mathbf{V}$ are then defined as

$$\mathbf{W}^T = \mathbf{\Sigma}_1^{-\frac{1}{2}}\mathbf{U}_1^T\mathbf{Z}_c^T \tag{33}$$

and

$$\mathbf{V} = \mathbf{Z}_o\mathbf{V}_1\mathbf{\Sigma}_1^{-\frac{1}{2}}. \tag{34}$$

A short calculation shows that the transformation with these matrices does in fact yield a system with a balanced realization.

In summary, in order to reduce the system by balanced truncation the observability and controllability Gramians are determined with the Lyapunov equations. Then a Cholesky decomposition is used to calculate the matrices $\mathbf{Z}_o$ and $\mathbf{Z}_c$ which in turn provide $\mathbf{V}$ and $\mathbf{W}$ via an additional SVD of the product $\mathbf{Z}_c^T \mathbf{Z}_o$.

4.2 Methodology

As described above, in order to perform a model order reduction, a full order model of the underlying problem is developed as a first step. For this purpose, it is necessary to know the exact system of differential equations of the detailed model which is defined in ANSYS Mechanical. Therefore, it is necessary to first extract all relevant equations from ANSYS Mechanical. These equations are implemented numerically in Python in a very similar way to the case of ANSYS. The demand here is that the final FOM (in Python) should provide the exact behavior of the original problem (described by ANSYS) with regard to user defined boundary conditions and precision. Hence, this model is verified against ANSYS Mechanical by comparison of both modal and transient analyses in the next step.

Once the FOM in Python has been verified, the dynamical system is reduced with the three methods presented in the previous paragraph. The reduced models will be compared to the full order model and to one another.

4.3 Extraction from ANSYS Mechanical and reduced order modelling

ANSYS Mechanical is a finite element software that was used to build and simulate the detailed model of fluid structure interactions. The dynamical system implemented in ANSYS Mechanical is a second order differential equation of the form:

$$\mathbf{M}\frac{\mathrm{d}^2}{\mathrm{d}t^2}\mathbf{x}(t) + \mathbf{D}\frac{\mathrm{d}}{\mathrm{d}t}\mathbf{x}(t) + \mathbf{K}\,\mathbf{x}(t) = \mathbf{q}(t) \tag{35}$$

$$\mathbf{y}(t) = \mathbf{C}\,\mathbf{x}(t). \tag{36}$$

In Eq. (35) $\mathbf{x}$ is the vector of the degrees of freedom (DOFs), $\mathbf{M}$ the mass matrix of the system, $\mathbf{D}$ the damping matrix, $\mathbf{K}$ the stiffness matrix and $\mathbf{q}$ represents the load vector. This system can be converted to a first order differential equation by setting

$$\mathbf{v}(t) := \frac{\mathrm{d}}{\mathrm{d}t}\mathbf{x}(t) \tag{37}$$

such that

$$\frac{d}{dt}\begin{pmatrix} \mathbf{x}(t) \\ \mathbf{v}(t) \end{pmatrix} = \begin{pmatrix} 0 & \mathbf{id} \\ -\mathbf{M}^{-1}\mathbf{K} & -\mathbf{M}^{-1}\mathbf{D} \end{pmatrix}\begin{pmatrix} \mathbf{x}(t) \\ \mathbf{v}(t) \end{pmatrix} + \begin{pmatrix} 0 \\ \mathbf{M}^{-1} \end{pmatrix}\mathbf{q}(t) \tag{38}$$

$$\mathbf{y}(t) = (\mathbf{C} \quad 0)\begin{pmatrix} \mathbf{x}(t) \\ \mathbf{v}(t) \end{pmatrix}. \tag{39}$$

Since all model order reduction techniques need the full equation of the dynamical system the system matrices and DOF maps had to be extracted from ANSYS Mechanical prior to model order reduction.

The degrees of freedoms in ANSYS Mechanical are organized in three different ways. The user ordering is the order which the user inputs in the setup of the model. The internal ordering is a compressed and reordered data format used for better cache performance. The last ordering is the solver ordering, which is optimized towards solver performance. These orderings are mapped onto each other with the NOD2SOLV matrix (which maps the solver ordering onto the internal ordering) and the BACK nodal mapping vector (to map the internal onto the user ordering). The mass and stiffness matrix are stored, according to the solver ordering of ANSYS Mechanical, in the binary full file.

All necessary matrices and vectors were exported to matrix market format from ANSYS Mechanical by adding the appropriate commands to the input script. After the export, all matrices were transferred to Python.
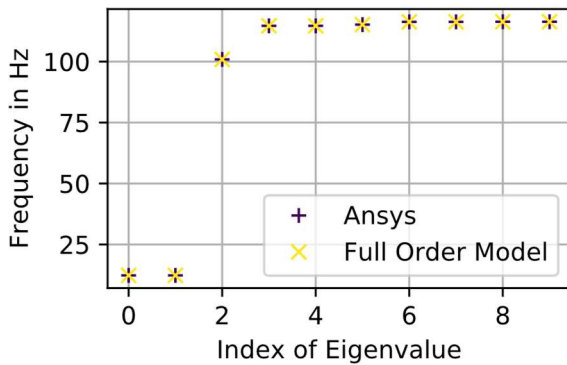
Figure 36: Comparison of eigenfrequencies between ANSYS Mechanical and FOM
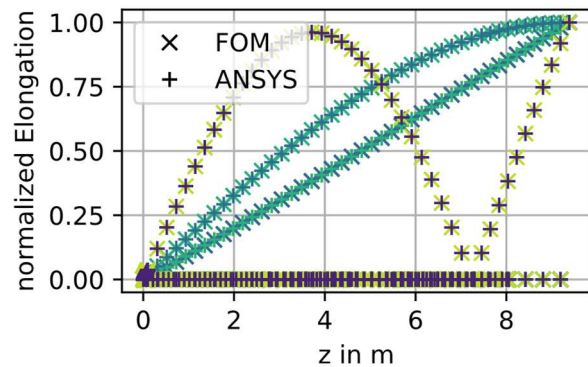
Figure 37: Comparison of the first four eigenmodes between ANSYS Mechanical and FOM

The Python model was, in a first step, verified via a comparison to the model from ANSYS Mechanical. The comparison of the eigenfrequencies and eigenmodes estimated with the 2 models is shown in Figure 36 and Figure 37, respectively. The full order model in Python agrees with ANSYS Mechanical and thus the transfer to Python was successful.

Time integration of ANSYS Mechanical is performed by Newmark time integration method (as a default) and optionally HHT-α integration method or backwards Euler time integration. These integrators were implemented into Python in order to achieve comparability also for the time integration.

The verified model of the system is then used to assess the three different model order reduction techniques. To this end, either the time series has to be reduced via SVD, in the case of POD or the full system matrix is reduced via the respective algorithms for Krylov subspace reduction and balanced truncation. These algorithms were either already available in Python (SVD, Cholesky decomposition) or were implemented for this purpose (Krylov subspace reduction). All the methods lead to low dimensional system matrices which are in turn used to construct the low dimensional reduced order model. Afterwards, the reduced order models are used to generate time series data. These are subsequently analyzed with different tools of signal analysis and compared both to the full order model and the ANSYS Mechanical model.

The system response to an initial deflection of the core barrel and the reactor pressure vessel bottom with no initial velocity, is evaluated with the ANSYS model, the FOM and the ROM. The deflection for one of the fuel assemblies in the x-direction, at middle elevation, is shown in Figure 38. For the comparison the option for large deflections was turned off in ANSYS and a numerical damping of γ=0.005 was selected.

As can be seen, there is a very good agreement of the full order model and ANSYS. The ROM used here was generated with the POD method with 20 modes. Figure 38 shows that in this case there is also a good agreement between the ROM and the FOM or ANSYS, respectively.
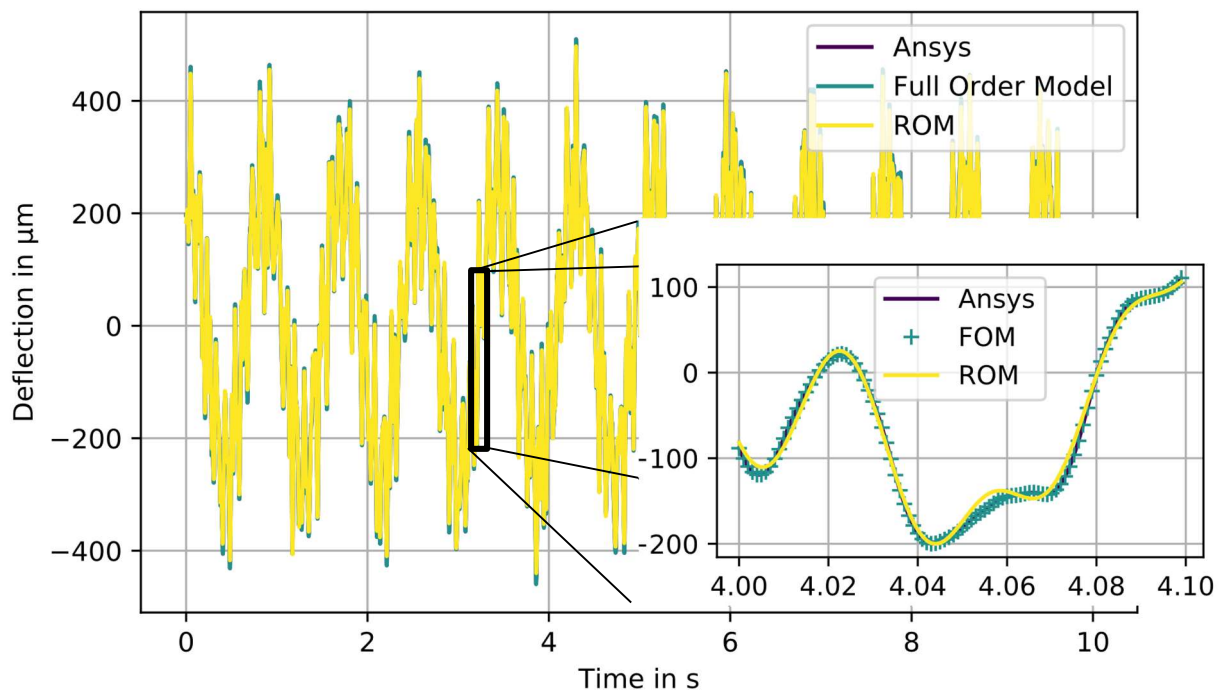
Figure 38: System response to a deflection of the core barrel and RPV; calculated time series of the deflection for a fuel assembly in the x-direction, at middle elevation

In Figure 39 the predicted signals are also compared in the frequency domain. In the relevant frequency range, there is a good agreement of the power spectral densities of all signals.

The reduction of the ANSYS model was therefore successful and the reduced model can be used for future investigations.
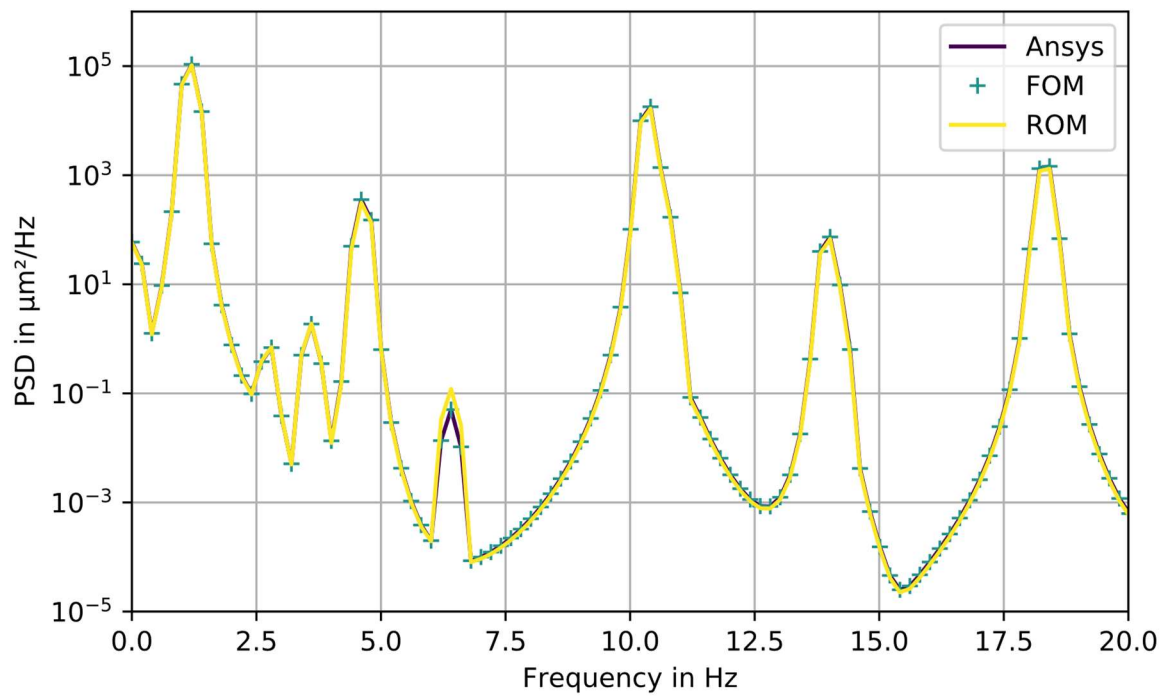
Figure 39: System response to a deflection of the core barrel and RPV; power spectrum density associated with the deflection for a fuel assembly in the x-direction, at middle elevation

5   Conclusion

Flow-induced mechanical oscillations can be a source of noise in neutron flux measurement in NPPs. A comprehensive overview of flow-induced mechanical oscillation phenomena with effect on neutron flux measurements is given in the report. Based on this work, a structure mechanical model has been developed, which allows the assessment of the dynamic behavior of the coupled system of RPV, core barrel and a row of fuel assemblies to given perturbations. The effects of the surrounding fluid are therein represented by added mass, stiffness and damping values as well as combined spring and damper elements. A first set of corresponding values is taken from investigations, which have been performed in conjunction with seismic analysis on single fuel assemblies in axial flow.

For a more versatile representation of the reactive fluid effects, an FSI-enhanced version of the system code ATHLET has been developed, which allows to modify the structure of the fluid domain and to calculate the feedback of the fluid to these changes.

The models have been tested in the frame of exemplary application cases and can be used in conjunction with the neutron kinetic code features developed within the CORTEX subtask 1.2 to compute the effect on neutron flux signals due to flow-induced vibrations.

Possible future improvements on the detailed mechanical model may concern the integration of the collisions between neighboring fuel assemblies. This might introduce a strong non-linearity into the model. Furthermore, additional oscillators like the primary cooling loop, further core internals or the remaining fuel assembly rows could be included. A long-term objective could be a fully integrated structural/hydraulic model of the reactor core.

Moreover, a methodology has been developed based on model order reduction techniques to transform the detailed model into reduced models for the integration into neutronic codes. The reduced model with the best performance will provide a basis for the implementation into the system codes. In correspondence with a possible future development of the detailed model, collisions of neighboring fuel assemblies may pose significant challenges for model order reduction techniques. The investigation of the limits of model order reduction methods in this case could provide more insight on the challenges of implementing FSI in existing system codes.

In the CORTEX subtask 4.2, parametric studies with the detailed model under different generic excitation conditions will be performed. After translating the results to neutron flux signals and comparing them to real plant data, further insights into the characteristics of neutron flux signals arising from flow-induced vibration phenomena could be obtained. In this way, the presented work contributes to the investigation of underlying phenomena for the temporary increase in low-frequency neutron flux in KWU type reactors between about 2000 and 2010.

6   Literature

Altstadt, E., Grunwald, G., Scheffler, M. & Weiß, F.-P., 1997. *Analytische Modellierung mechanischer Schwingungen von Primärkreiskomponenten des Druckwasserreaktors WWER-440 mit finiten Elementen,* s.l.: Forschungszentrum Rossendorf, FZR-172.

Altstadt, E. & Weiss, F.-P., 1999. *Finite Element based vibration analysis of WWER-440 type reactors,* s.l.: Annals of Nuclear Energy, Vol. 26, pp. 1037-1052.

Antoulas, A. C., Sorensen, D. C. & Gugercin, S., 2001. *A survey of model reduction methods for large-scale systems,* s.l.: American Mathematical Society, vol. 280, pp. 193–219.

Austregesilo, H. et al., 2019. *ATHLET 3.2 Models and Methods (GRS-P-1/Vol. 4 Rev. 5),* s.l.: GRS gGmbH.

Au-Yang, M. K., Brenneman, B. & Raj, D., 1995. *Flow-induced vibration test of an advanced water reactor model - Part 1: turbulence-induced forcing function,* s.l.: Nuclear Engineering and Design, Vol. 157, pp. 93-109.

Bai, Z., 2002. *Krylov subspace techniques for reduced-order modeling of large-scale dynamical systems,* s.l.: Applied Numerical Mathematics, vol. 43, no. 1–2, pp. 9–44.

Banyay, G. A., Imbrogno, G. M. & Meyer, G. A., 2013. *Generation of Pump-Induced Pulsation Loads For the AP1000 Reactor Internals,* San Francisco, USA: Transactions of the SMiRT-22 Conference.

Banyay, G. A. & Meyer, G. A., 2014. *Synopsis - The Comprehensive Vibration Assessment Program (CVAP) for AP1000 Reactor Internals,* s.l.: Presentation at the CAV workshop.

Bauernfeind, V., 1977. *Investigations on the Vibrative Excitation of PWR Pressure Vessel and Internals by Pressure Noise Analysis and Model Calculations,* s.l.: Progress in Nuclear Energy, Vol. 1, pp. 323-332.

Bauernfeind, V., 1988. *Vibration Monitoring of a Four-Loop PWR: Model-Investigations of the Sensitivity of the Monitored Signals on Mechanical Failures,* s.l.: Progress in Nuclear Energy, Vol. 21, pp. 247-254.

Baur, U., Benner, P. & Feng, L., 2014. *Model Order Reduction for Linear and Nonlinear Systems: A System-Theoretic Perspective,* s.l.: Arch. Comput. Methods Eng., vol. 21, no. 4.

Benner, P., Gugercin, S. & Willcox, K., 2013. *A survey of model reduction methods for parametric systems,* s.l.: MPI Magdeburg Prepr., vol. MPIMD, no. 13–14, pp. 1–36.

Billerey, A., 2005. *Evolution of Fuel Rod Support under Irradiation - Impact on the Mechanical Behaviour of Fuel Assemblies,* s.l.: Proceedings of a technical meeting held in Cadarache, France, 22–26 November 2004, IAEA-TECDOC-1454.

Borsoi, L., 2001. *Flow-Induced Vibration of Nuclear Components - Future R&D Perspective Derived from the French Experience,* Washington DC: Transactions of the SMiRT 16 Conference.

Broc, D., Queval, J. C. & Viallet, E., 2003. *Seismic Behaviour of a PWR Reactor Core: Fluid Structure Interaction Effects,* Prague: Transactions of the 17th SMiRT Conference.

Chen, C.-T., 1998. *Linear System Theory and Design, 3rd ed.,* New York, NY, USA: Oxford University Press, Inc..

Collard, B., 2004. *Flow Induced Damping of a PWR Fuel Assembly,* s.l.: Proceedings of a technical meeting held in Cadarache, France, IAEA-TECDOC-1454.

Corves, B., 2010. *Grundlagen der Maschinen und Strukturmechanik,* s.l.: RWTH Aachen.

Dach, K. et al., 1985. *The Experiences of Using Neutron Noise Analysis For Vibration Behaviour of Internal Structures,* s.l.: Progress in Nuclear Energy, Vol. 15, pp. 243-250.

Damiano, B. & Kryter, R. C., 1990. *Current Applications of Vibration Monitoring and Neutron Noise Analysis,* s.l.: Oak Ridge National Laboratory, NUREG/CR-5479.

Demazière, C., 2017. *Neutron noise-based core monitoring for identifying and characterizing anomalies and their root causes in operating reactors,* Berlin: Presentation at the 2017 Annual Meeting on Nuclear Technology.

Elmahdi, A. M. et al., 2011. *Flow Induced Vibration Forces on a Fuel Rod by LES CFD Analysis,* Ontario: NURETH-14 Conference.

Feldmann, P. & Freund, R. W., 1995. *Efficient Linear Circuit Analysis by Padé Approximation via the Lanczos Process,* s.l.: IEEE Trans. Comput. Des. Integr. Circuits Syst., vol. 14, no. 5, pp. 639–649.

Fiedler, J., 2002. *Schwingungsüberwachung von Primärkreiskomponenten in Kernkraftwerken,* s.l.: Dissertation, University of Hannover.

Fontaine, B. & Politopoulos, I., 2000. *A non linear model for the PWR fuel assembly seismic analysis,* s.l.: Nuclear Engineering and Design, Vol. 195, pp. 321-329.

Fry, D. N., Kryter, R. C. & Robinson, J. C., 1974. *Analysis of Neutron Density Oscillations Resulting from Core Barrel Motion in the Palisades Nuclear Power Plant,* s.l.: Oak Ridge National Laboratory, ORNL-TM -4570.

Fry, D. N., March-Leube, J. & Sweeney, F. J., 1984. *Use of Neutron Noise for Diagnosis Of In-Vessel Anomalies in Light-Water Reactors,* s.l.: Union Carbide Corporation, NUREG/CR-3303.

Fujita, K., 1990. *Flow-Induced Vibration and Fluid-Structure Interaction in Nuclear Power Plant Components,* s.l.: Journal of Wind Engineering and Industrial Aerodynamics, Vol. 33, pp. 405-418.

Glösmann, P. & Kreuzer, E., 2005. *Nonlinear system analysis with Karhunen-Loève transform,* s.l.: Nonlinear Dyn., vol. 41, no. 1–3, pp. 111–128.

Haslinger, K. H., Joffre, P. F., Nordström, L. & Andersson, S., 2001. *Flow Induced Vibration Testing of a PWR Fuel Assembly,* Washington DC: Transactions of the SMiRT 16 Conference.

Herb, J., 2019. *Coupled OpenFOAM-ATHLET simulations of the primary circuit of a liquid sodium cooled reactor,* Duisburg, Germany: 14th OpenFOAM® Workshop.

Herb, J., Bläsius, C. & Küntzel, M., 2016. *Untersuchungen der Ursachen für Neutronenflussschwankungen,* s.l.: Abschlussbericht zum Vorhaben RS 1533, GRS - 408, ISBN 978-3-944161-90-7.

Herb, J. et al., 2017. *Analyses of Possible Explanations for the Neutron Flux Fluctuations in German PWR,* Berlin: 48th Annual Meeting on Nuclear Technology.

Hollstein, F., 1995. *Berechnung von Neutronenflußdichteschwankungen in WWER-Druckwasserreaktoren infolge strömungsinduzierter Schwingungen,* s.l.: Forschungszentrum Rossendorf, FZR-110.

Horváth, Á. & Dressel, B., 2013. *On numerical simulations of fuel assembly bow in pressurized water reactors,* s.l.: Nuclear Engineering and Design, Vol. 265, pp. 814-825.

Jeon, S. Y. et al., 2009. *An Investigation on the Fuel Assembly Structural Performance for the PLUS7 Fuel Design,* Espoo, Finland: 20th SMiRT Conference.

Kaneko, S. e. a., 2014. *Flow-Induced Vibrations - Classifications and Lessons from Practical Experiences,* s.l.: Elsevier, ISBN: 978-0-08-098347-9.

Kim, H. K. et al., 2012. *Development of Fuel Rod Vibration and Fluid Elastic Instability Analysis Code: ROVIN,* Manchester, UK: Transactions of the 2012 TopFuel Conference.

Kommajosyula, R. & Xiao, X., 2014. *ATHLET Framework for Embedding/ Extending: An Efficient, Flexible & Easy-to-use Python Framework to a Large FORTRAN Code,* Passau, Germany: 5th IEEE Germany Student Conference, IEEE GSC 2014.

Laggiard, E. et al., 1995. *Vibration Measurement in PWR Obrigheim by Use of In-Core Accelerometers,* s.l.: Progress in Nuclear Energy, Vol. 29, No. 3/4, pp. 229-238.

Langenbuch, S. & Velkov, K., 2005. *Overview on the development and application of the coupled code system ATHLET-QUABOX/CUBBOX,* Avignon, France: Proceedings of Mathematics and Computation, Supercomputing, Reactor Physics and Nuclear and Biological Applications.

Langenbuch, S., Velkov, K. & Lizorkin, M., 1997. *3D neutronic codes coupled with thermal-hydraulic system codes for PWR, and BWR and VVER reactors,* s.l.: Proceedings of the OECD/CSNI workshop on transient thermal-hydraulic and neutronic codes requirements, pp. 506–524..

Lenaerts, V., Kerschen, G. & Golinval, J. C., 2001. *Proper orthogonal decomposition for model updating of non-linear mechanical systems,* s.l.: Mech. Syst. Signal Process., vol. 15, no. 1, pp. 31–43.

Lerchl, G. et al., 2019. *ATHLET 3.2 User's Manual. GRS (GRS-P-1/Vol. 1 Rev. 8),* s.l.: GRS gGmbH.

Liewers, P., Schmitt, W., Schumann, P. & Weiss, F. P., 1988. *Detection of Core Barrel Motion at WWER-440-Type Reactors,* s.l.: Progress in Nuclear Energy, 1988, Vol. 21, pp. 89-96..

Lu, R. Y. & Seel, D. D., 2006. *PWR Fuel Assembly Damping Characteristics,* Miami, USA: Proceedings of ICONE 14.

Manthey, R., Knospe, A., Lange, C. & Hennig, D., 2017. *Reduced order modeling of natural circulation system by proper orthogonal decomposition,* s.l.: s.n.

Mitzel, F., Väth, W. & Ansari, S., 1982. *Nachweis von Brennelementschwingungen in KNK II,* s.l.: Kernforschungszentrum Karlsruhe, KfK 3379.

Mulcahy, T. M., 1983. *A review of leakage-flow-induced vibrations of reactor components,* s.l.: Argonne National Laboratory, ANL--83-43.

O'Cain, M. B., 2013. *Root Cause Analysis Summary - Krsko Cycle 26 Leaking Fuel Assemblies,* s.l.: CAPS 13-282-C025.

Païdoussis, M., 2016. *Fluid-Structure Interactions - Slender Structures and Axial Flow,* s.l.: Elsevier Ltd., ISBN 978-0-12-397333-7.

Païdoussis, M. P., 2006. *Real-life experiences with flow-induced vibration,* s.l.: Journal of Fluids and Structures, Vol. 22, pp. 741–755.

Palamera, M. J. et al., 2015. *Development of an advanced PWR reactor Internals System Finite Element Model for Flow-Induced Vibration Analysis,* s.l.: Proceedings of the ASME 2015 Pressure Vessels and Piping Conference, PVP2015-45278.

Perin, Y., Velkov, K., Pasichnyk, I. & Langenbuch, S., 2012. *Rod Ejection Accident by the Coupled System Code ATHLET-QUABOX/CUBBOX,* s.l.: Journal of Power and Energy Systems, Vol. 6, No. 2, pp. 165-176.

Pettigrew, M. J. et al., 1998. *Flow-induced vibration: recent findings and open questions,* s.l.: Nuclear Engineering and Design, Vol. 185, pp. 249–276.

Pisapia, S., Collard, B., Bellizi, S. & Mori, V., 2003. *Modal Testing and Identification of a PWR Fuel Assembly,* Prague: Transactions of the 17th SMiRT Conference.

Pohlus, J. & Paquée, U., 2018. *Untersuchung veränderter Neutronenflussschwankungen und Brennstab-Beanspruchungen in DWR-Anlagen im Rahmen der Sicherheitsforschung,* s.l.: TÜV Rheinland ISTec GmbH, ISTec - A – 3695.

Prill, D. P. & Class, A. G., 2014. *Semi-automated proper orthogonal decomposition reduced order model non-linear analysis for future BWR stability,* s.l.: Ann. Nucl. Energy, vol. 67, pp. 70–90.

Reaktorsicherheitskommission, 2013. *Stellungnahme DWR-Neutronenflussschwankungen,* s.l.: 457. Sitzung vom 11.04.2013.

Reavis, J. R., 1969. *Vibration Correlation for Maximum Fuel-Element Displacement in Parallel Turbulent Flow,* s.l.: Nuclear Science and Engineering, Vol. 38, pp. 63-69.

Rega, G. & Troger, H., 2005. *Dimension reduction of dynamical systems: Methods, models, applications,* s.l.: Nonlinear Dyn., vol. 41, no. 1–3, pp. 1–15.

Ricciardi, G., 2016. *Fluid–structure interaction modelling of a PWR fuel assembly subjected to axial flow,* s.l.: Journal of Fluids and Structures, Vol. 62, pp. 156-171.

Ricciardi, G., 2017. *Dynamical Nonlinear Modelling Of A Pressurised Water Reactor Fuel Assembly Subjected To An Axial Flow,* s.l.: 10th International Conference on Structural Dynamics, EURODYN.

Ricciardi, G., Bellizzi, S., Collard, B. & Cochelin, B., 2009. *Modelling Pressurized Water Reactor Cores in Terms of Porous Media,* s.l.: Journal of Fluids and Structures, Vol. 25, pp. 112-133.

Ricciardi, G., Bellizzi, S., Collard, B. & Cochelin, B., 2009. *Row of fuel assemblies analysis under seismic loading: modelling and experimental validation,* s.l.: s.n.

Ricciardi, G. & Boccaccio, E., 2015. *Modelling of the flow induced stiffness of a PWR fuel assembly,* s.l.: Nuclear Engineering and Design, Vol. 282, pp 8-14.

Rigaudeau, J., Brochard, D. & Benjedidia, A., 1993. *Fluid Structure Interaction in the Response of PWR Fuel Assemblies to Horizontal Seismic Loads,* s.l.: Transactions of the SMiRT-12 Conference.

Runkel, J., 1987. *Rauschanalyse in Druckwasserreaktoren,* s.l.: Dissertation, University of Hannover.

Runkel, J., Laggiard, E., Stegemann, D. & Heidemann, P., 1995. *In-Core Measurements of Reactors Internals Vibrations by Use of Accelerometers and Neutron Detectors,* s.l.: Institute of Nuclear Engineering and Non-destructive Testing.

Salimbahrami, B. & Lohmann, B., 2002. *Krylov subspace methods in linear model order reduction: Introduction and invariance properties,* s.l.: Sci. Rep. Inst. Autom., pp. 1–11.

Scheuer, J., 2019. *Fortran Development Extensions (libfde),* s.l.: https://github.com/Zorkator/libfde, last checked 04/11/2019.

Schumann, P., 2000. *Nutzung der Rauschdiagnostik für Nachweis und Überwachung der Schwingungen von Reaktordruckbehältereinbauten und zur Aufklärung ihrer Ursachen in ostdeutschen Kernkraftwerken mit WWER-440/230-Reaktoren der russischen Baureihe,* s.l.: Forschungszentrum Rossendorf, FZR-304.

Seidel, M., Kosowski, K., Schüler, U. & Belblidia, L., 2015. *Review of the historic neutron noise behavior in German KWU built PWRs,* s.l.: Progress in Nuclear Energy, Vol. 85, pp. 668-675.

Shah, S. J., Brenneman, B. & Rigadeau, J., 2001. *Comparison of Analytical and Experimental Damping Under Axial Flow for Different Fuel Assembly Types,* Nice: 9th International Conference on Nuclear Engineering.

Snyder, M., 2004. *Method for Hydrodynamic Coupling of Concentric Cylindrical Shells and Beams,* s.l.: s.n.

Snyder, M. et al., 2004. *Progress in the Generation of Flow Turbulence Excitation Forces from CFD Analyses and Experimental Data,* Nara, Japan: Paper ID 0000127, NUTHOS-6 Conference.

Snyder, M. et al., 2003. *AP1000 Reactor Internals Flow-Induced Vibration Assessment Program,* s.l.: AP1000 Document: APP-MIO1-GER-001, Revision 1.

Stabel, J., Ren, M. & Ladouceur, B., 2005. *New Knowledge and Experiences of Flow Induced Fretting in PWR Fuel Assemblies,* s.l.: SMiRT 18 Conference.

Stegemann, D. & Runkel, J., 1995. *Experience with Vibration Monitoring in German PWRs Obrigheim, Grohnde, Brokdorf and Emsland,* s.l.: Institute of Nuclear Engineering and Nondestructive Testing, IKPH, University of Hannover.

Sunder, R., 1985. *Sammlung von Signalmustern zur DWR Schwingungsüberwachung - Informationsgehalt der Neutronenflussrauschsignale,* s.l.: GRS-A-1074.

Thie, J. A., 1981. *Power Reactor Noise,* s.l.: La Grange Park: American Nuclear Society.

Thompson, J. P., McCoy, G. R. & Lubin, B. T., 1980. *Experimental Value of Percent Variation in Root-Mean-Square Ex-Core Detector Signal to the Core Barrel Amplitude Scale Factor,* s.l.: Nuclear Technology, Vol. 48:2, pp. 122-127.

Trenty, A., 1995. *Operational Feedback on Internal Structure Vibration in 54 French PWRs during 300 Fuel Cycles,* s.l.: s.n.

Viallet, E. et al., 2003. *Validation of PWR Core Seismic Models with Shaking Table Tests on Interacting Scale 1 Fuel Assemblies,* Prague: Transactions of the 17th SMiRT Conference.

Viallet, E. & Kestens, T., 2003. *Prediction of Flow Induced Damping of a PWR Fuel Assembly in Case of Seismic and Loca Load Case,* Prague: Transactions of the SMiRT-17 Conference.

Viebach, M. et al., 2018. *Frequency-Domain Investigation on the Neutron Noise in KWU PWRs,* s.l.: 49th Annual Meeting on Nuclear Technology.

Wach, D. & Sunder, R., 1977. *Improved PWR-Neutron Noise Interpretation Based on Detailed Vibration Analysis,* s.l.: Progress in Nuclear Energy. Vol. 1, pp. 309-322.

Wach, D. & Sunder, R., 1988. *Long-Term Vibration Trending as a Basis for Performance Assessment and Life Extension of Mechanical Components,* s.l.: Gesellschaft für Reaktorsicherheit (GRS) mbH.

Wanninger, A., Seidel, M. & Macián-Juan, R., 2016 b. *Screening sensitivity analysis of a PWR fuel assembly FEM structural model,* s.l.: Top Fuel 2016 Conference.

Wanninger, A., Seidl, M. & Macián-Juan, R., 2016 a. *Development of computational methods to describe the mechanical behavior of PWR fuel assemblies,* Hamburg: 47th Annual Meeting on Nuclear Technology.

Wehling, H. J., Klinger, K. & Stölben, H., 1985. *The Influence of Thermohydraulic Parameters on the Dynamic Behaviour of KWU-PWR's,* s.l.: Progress in Nuclear Energy, Vol. 15, pp. 273-282.

Wei, Z., 2015. *Predictive Study of CAP1400 Core Barrel Flow-induced Vibration Part 1: Turbulence induced Forcing Function,* Manchester: Transactions of the SMiRT-23 Conference.

Witters, F., 2004. *Fluid Damping on Fuel Assemblies under Axial Flow,* s.l.: Proceedings of a technical meeting held in Cadarache, France, IAEA-TECDOC-1454.

Yun Je, S., Chang, Y. S. & Kang, S. S., 2017. *Dynamic characteristics assessment of reactor vessel internals with fluid-structure interaction,* s.l.: Nuclear Engineering and Technology, Vol. 49, pp. 1513-1523.

Zeman, V. & Hlavác, Z., 2008. *Dynamic Response of VVER 1000 Type Reactor Excited by Pressure Pulsations,* s.l.: Engineering Mechanics, Vol. 15, No. 6, pp. 435–446.

Appendix A Mathematical expression of idealized FA bending modes
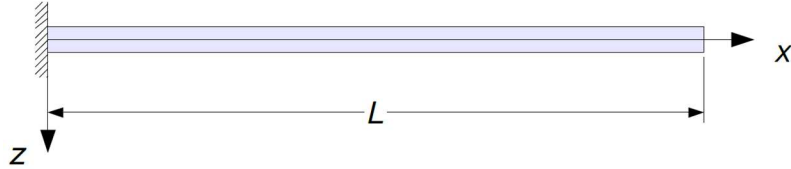
Cantilevered beam mode

Figure 40: Schematic representation of the cantilevered beam mode

General equation, where ν is the mode number:

$$z(x) = \cos(\kappa_\nu x) - \cosh(\kappa_\nu x) - \gamma_\nu(\sin(\kappa_\nu x) - \sinh(\kappa_\nu x)) \qquad (A-1)$$

with

$$\gamma_\nu = \frac{\cos(\kappa_\nu L) + \cosh(\kappa_\nu L)}{\sin(\kappa_\nu L) + \sinh(\kappa_\nu L)} \qquad (A-2)$$

$$\kappa_1 \approx \frac{1.8751}{L}, \kappa_2 \approx \frac{4.6941}{L}, \kappa_3 \approx \frac{7.8548}{L}, \kappa_4 \approx \frac{10.996}{L}, \kappa_\nu \approx (2\nu - 1)\frac{\pi}{2L} \qquad (A-3)$$

First mode:

$$z(x) \approx \cos\left(1.8751\frac{x}{L}\right) - \cosh\left(1.8751\frac{x}{L}\right) - 0.7341\left(\sin\left(1.8751\frac{x}{L}\right) - \sinh\left(1.8751\frac{x}{L}\right)\right) \qquad (A-4)$$
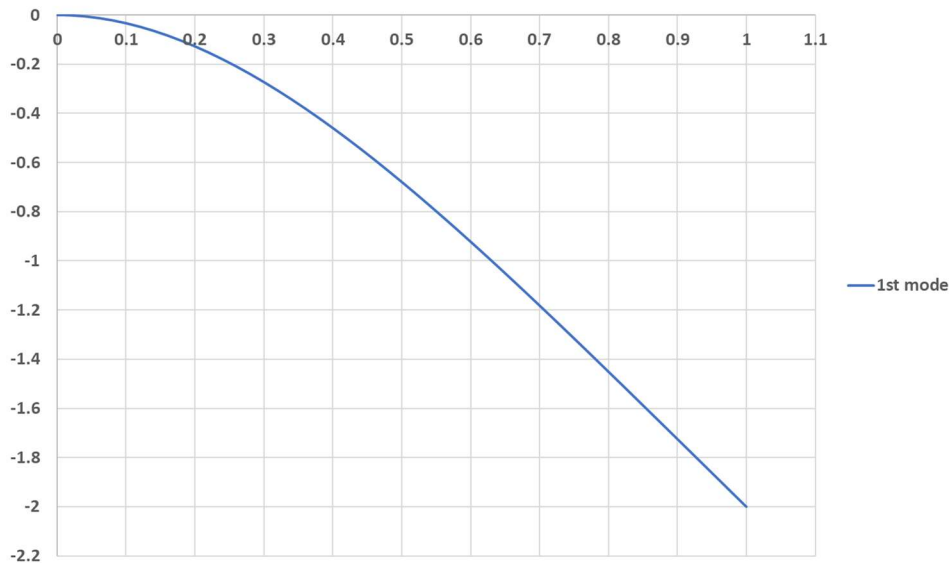

Figure 41: Graph describing the deflection of the cantilevered beam mode
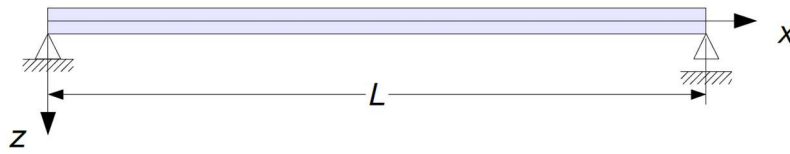
Simply supported on both sides

Figure 42: Schematic representation of a beam simply supported on both sides

General equation, where ν is the mode number:

$$z(x) = \sin(\kappa_\nu x) \qquad (A-5)$$

with

$$\kappa_\nu = \nu \frac{\pi}{L} \qquad (A-6)$$

First mode:

$$z(x) = \sin\left(\pi \frac{x}{L}\right) \qquad (A-7)$$

Second mode:
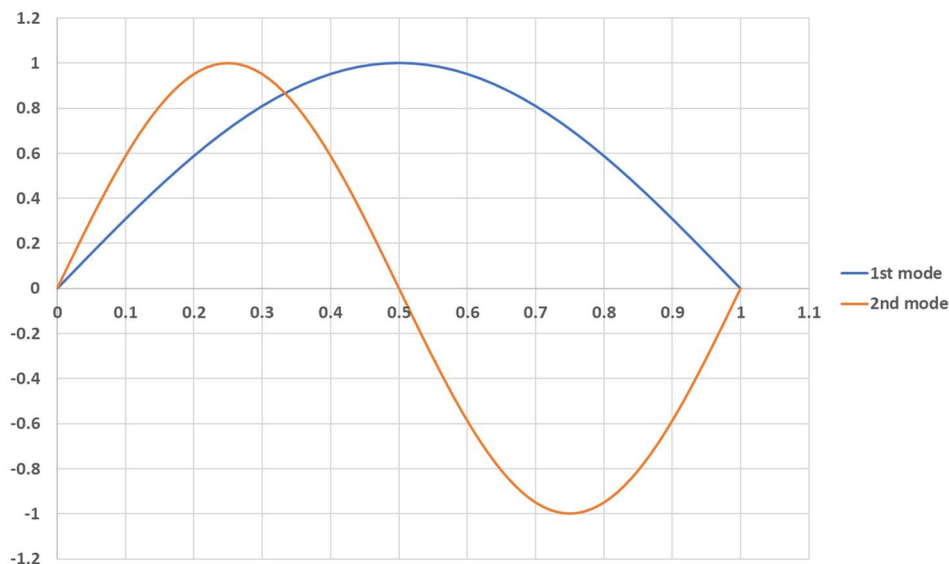
$$z(x) = \sin\left(2\pi \frac{x}{L}\right) \qquad (A-8)$$

Figure 43: Graph describing the deflection of the beam mode simply supported on both sides
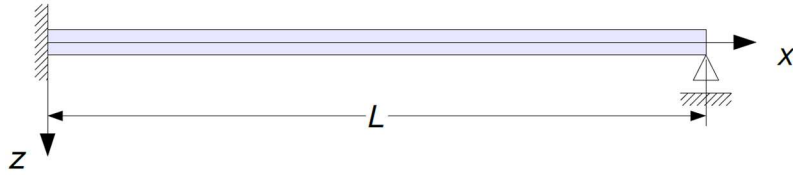
Cantilevered beam additionally simply supported

Figure 44: Schematic representation of a cantilevered beam additionally simply supported

General equation, where ν is the mode number:

$$z(x) = \cos(\kappa_\nu x) - \cosh(\kappa_\nu x) - \gamma_\nu(\sin(\kappa_\nu x) - \sinh(\kappa_\nu x)) \qquad (A-9)$$

with

$$\gamma_\nu = \frac{\cos(\kappa_\nu L) + \cosh(\kappa_\nu L)}{\sin(\kappa_\nu L) + \sinh(\kappa_\nu L)} \qquad (A-10)$$

$$\kappa_\nu \approx (2\nu - 1)\frac{\pi}{2L} \qquad (A-11)$$

First mode:

$$z(x) \approx \cos\left(3.9266\frac{x}{L}\right) - \cosh\left(3.9266\frac{x}{L}\right) - 1.0007\left(\sin\left(3.9266\frac{x}{L}\right) - \sinh\left(3.9266\frac{x}{L}\right)\right) \qquad (A-12)$$

Second mode:

$$z(x) \approx \cos\left(7.0686\frac{x}{L}\right) - \cosh\left(7.0686\frac{x}{L}\right) - \left(\sin\left(7.0686\frac{x}{L}\right) - \sinh\left(7.0686\frac{x}{L}\right)\right) \qquad (A-13)$$
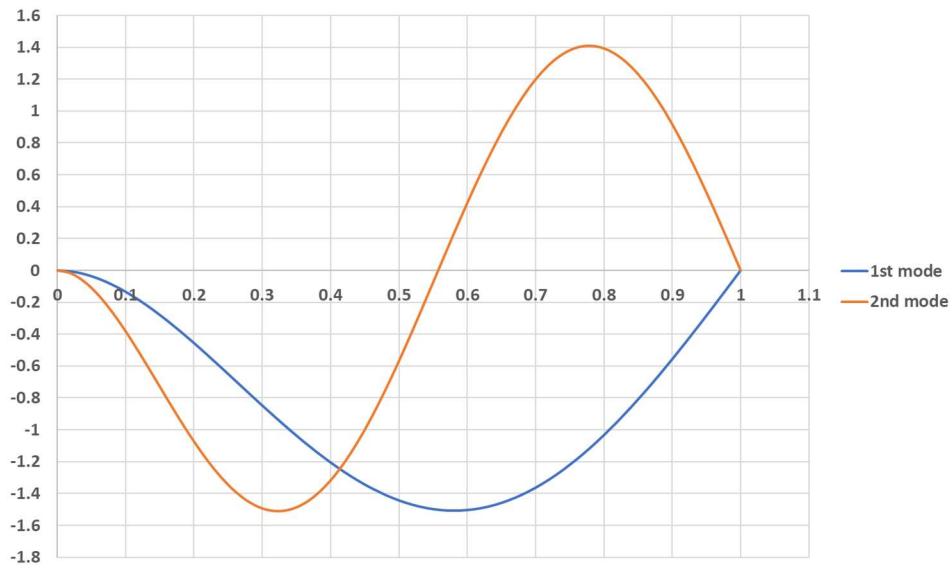

Figure 45: Graph describing the deflection of the cantilevered beam mode additionally simply supported